筑　波　大　学

博 士 （医 学） 学 位 論 文

Role of *Tet2*-deficient immune cells in lung cancer - a model of clonal hematopoiesis-derived immune cells in solid cancers
(肺がんにおける *Tet2* 機能欠失免疫細胞の意義 – 固形がんにおけるクローン性造血由来免疫細胞のモデル)

2021

筑波大学大学院博士課程人間総合科学研究科

Nguyen Thi Minh Yen

TABLE OF CONTENTS

LIST OF ABBREVIATIONS

CH	**Clonal hematopoiesis**
HSCs/HSPCs	**Hematopoietic stem/progenitor cells**
TME	**Tumor microenvironment**
MDSC	**Myeloid-derived suppressor cells**
TAM	**Tumor-associated macrophages**
NK	**Natural killer cells**
DC	**Dendritic cells**
MDSC	**G-MDSC Granulocytic**
qPCR	**Quantitative RT-PCR**
GMD	**Granulocytic myeloid-derived cells**
MMD	**Monocytic myeloid-derive cells**
LLC	**Lewis Lung Carcinoma**
PBS	**Phosphate buffered saline**
RPMI	**Roswell Park Memorial Institute**
DMEM	**Dulbecco's Modified Eagle's Medium/high glucose**
FCS	**Fetal calf serum**
PS	**Penicillin-Streptomycin Solution**
WTA	**Whole transcriptome analysis**
DEGs	**Differentially expressed genes**
scRNA-seq	**Single cell RNA sequencing**
CCA	**Canonical correlation analysis**
PCA	**Principal component analysis**
UMAP	**Uniform Manifold Approximation and Projection**
ELISA	**Enzyme-linked immune sorbent assay**
RT	**Room temperature**
HE	**Hematoxylin and eosin**

LIST OF TABLES AND FIGURES

1. BACKGROUND

1.1 Clonal hematopoiesis

In hematopoietic system most of mature blood cells are generated from hematopoietic stem cells and contribute to innate and adaptive responses[1]. Somatic mutations occur during the cell division processes [1]. The status in which hematopoietic cells harboring these somatic mutations are expanded is called as "clonal hematopoiesis" (CH) [1, 2, 3] (Fig. 1). In aging, the hematopoietic system undergoes gradual replacement via "CH", in which hematopoietic stem/progenitor cells (HSCs/HSPCs) acquire somatic mutations, clonally expand, and continuously differentiate into various lineages of blood cells harboring those mutations [2, 3]. In healthy individuals, the frequency of clonal hematopoiesis gradually increases with age, and is reportedly ~10% in the 60s, 20% in the 70s, and 30% in the 80s [2, 3], [4].

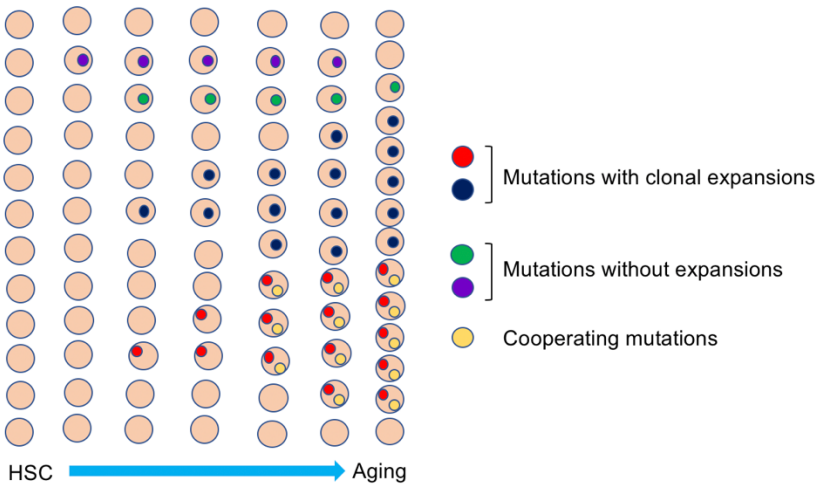

Figure 1. The evolution of CH in aging

1.2 Tumor microenvironment

Tumor microenvironment (TME) is typically formed from a complex of immune cells, including B and T lymphocytes, myeloid-derived suppressor cells (MDSC), tumor-associated macrophages (TAM), natural killer cells (NK), dendritic cells (DC) and so forth, and non-immune cells. One of the main functions of TME is to regulate cancer progression via operating immune responses, thus influencing the efficacy of cancer treatment [5].

Microenvironmental cells promote cancer progression by either directly supporting tumor growth or suppressing an anti-cancer immune response [6]. Immune cells including TAM and MDSC are critical components of the cancer microenvironment [5, 6]. Both are derived from hematopoietic stem/progenitor cells in bone marrow, some of which undergo differentiation in spleen, and finally migrate and infiltrate into cancer tissues.

1.3 CH mutations in non-hematologic malignancies

Besides understanding of the prevalence and clinical implications of CH in patients with hematologic malignancies, CH is related to reducing overall survival and elevating risk of cardiovascular mortality [2, 3]. Further, the frequency of CH was reported to be as high as 25% in patients with solid cancers in a study including >8,000 patients with various types of solid cancers, such as lung, urogenital, and gastro-intestinal cancers

[7, 8]. Moreover, mutations in genes functioning in epigenetic pathways (*DNMT3A*, *TET2*, and *ASXL1*) and in the p53 pathway (*PPM1D* and *TP53*) account for up to 50% of CH in patients with solid cancers [7]. Thus, a proportion of immune cells in the cancer microenvironment presumably have somatic mutations identical to those in CH [9].

Several studies have reported activities of these immune cells using mouse models. For example, it was shown that melanoma progression is suppressed in a myeloid-specific *Tet2*-deficient model due to increased T-cell recruitment [10], while liver cancer progression was enhanced in a systemic *Tet2*-deficient model due to expansion of granulocytic MDSC (G-MDSC) and decreased T-cell recruitment [11]. Nonetheless, in most types of cancers it remains unclear how immune cells with somatic mutations function in cancer progression.

2. RESEARCH PURPOSES AND OBJECTIVES

Ten-Eleven-Translation-2 (TET2), one of members in TET family is known as a key tumor suppressor in the hematopoietic system via regulating DNA methylation [10, 12, 13]. *TET2* somatic mutations are one of most frequent clonal expansions besides *DNMT3A* [3, 4, 7]. *TET2*-deficency-driven CH is suggested as causing myeloid cancers or lymphoid cancers [12] or supporting insulin resistance in aging and obesity [14]. It is still unclear how *TET2*-mutated immune cells derived from CH function as microenvironmental cells in solid cancer development. In this study, therefore, I focused on the role of *Tet2*-deficient immune cells in lung cancer development using murine models (Fig. 2).

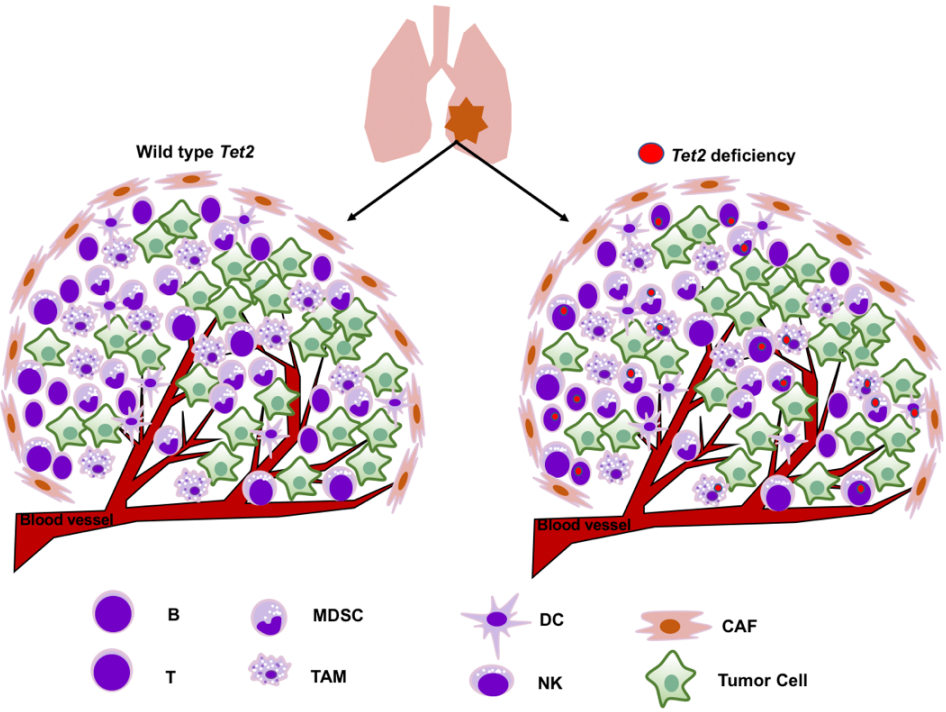

Figure 2. TME with non-mutation immune cells and CH-harboring immune cells.

According to this, I targeted to 3 objectives:

- Evaluate tumor growth in a *Tet2*-deficent mice comparing with wild type mice.
- Determine mediators and their pathway supporting for tumor progression.
- Find a new immune therapy targeting to mediator signaling in cancer treatment.

3. MATERIALS AND METHODS

3.1 Mice

Tet2$^{flox/flox}$ mice [13] were crossed with *Mx-Cre* mice [15] to generate *Mx-Cre* x *Tet2*$^{flox/flox}$ mice. Polyinosinic: polycytidylic (pIpC) (Sigma, code# P0913) was intraperitoneally injected into *Mx-Cre* x *Tet2*$^{flox/flox}$ and *Tet2*$^{flox/flox}$ mice at a dose of 300 μg/mouse every 2 days from day 2 after birth with 3 doses in total. *Tet2* gene is assumed to be disrupted in all hematopoietic cells in pIpC-treated *Mx-Cre* x *Tet2*$^{flox/flox}$ mice. These mice are referred to as *Tet2*$^{-/-}$ and *Tet2*$^{+/+}$ mice, respectively. *Tet2*$^{flox/flox}$ mice were also crossed with *LysM-Cre* mice (Strain #004781), purchased from Jackson laboratory to obtain *Tet2*$^{flox/flox}$ x *LysM-Cre* (*Tet2*$^{mye-/-}$) mice, which show *Tet2* disruption specifically in myeloid cells. *Tet2*$^{flox/flox}$ mice (*Tet2*$^{mye+/+}$) were used as control. Female mice 6-8 weeks old were used for all experiments.

This research was approved by the Facility Review Committee of the Laboratory Animal Resource Center, University of Tsukuba. All mouse experiments were performed following guidelines of the Laboratory Animal Resources Center.

3.2 Lung cancer cell lines

Lewis Lung Carcinoma (LLC) cells purchased from RIKEN BRC were cultured in Dulbecco's Modified Eagle's Medium/high glucose (DMEM) (Sigma-Aldrich, code# D5796) supplemented with 10% fetal calf serum (FCS) (Bioser, code# 554-02155) and 1% Penicillin-Streptomycin Solution (PS) (Wako, code# 168-23191). LLC cells were then expanded to enable injection into mice and for use in in vitro experiments. LLC cells within 4 - 10 passages were used for experiments.

The human lung cancer lines LC-Ad-1 and A549 were cultured in Roswell Park Memorial Institute (RPMI) (Sigma-Aldrich, code# r8758) plus 10% FCS and 1% PS. One week after thawing, these cell lines that had been passaged more than 4 times were used for S100A8/A9 stimulation experiments.

3.3 Subcutaneous transplantation of LLC cells into the flank of mice

Tet2$^{-/-}$ and *Tet2*$^{+/+}$ mice or *Tet2*$^{mye-/-}$ and *Tet2*$^{mye+/+}$ mice were injected with $2x10^5$ LLC cells in 100 μL of phosphate buffered saline (PBS) (Nissui, code# 5913) subcutaneously at flanks. Tumor volume was measured every 2 days after injection by calipers and calculated as length x width x width x 0.52.

3.4 Single cell suspensions from tumors

Tumors were resected at day 18, or when the largest tumors reached 1000 mm^3. Tumors were first minced with surgical scissors and the digested enzymatically for 30 minutes at 37^o in 5 mL RPMI medium supplemented with 10% FCS and containing 0.75 mg/mL collagenase type IV (Gibco, 17104-019) and 0.05 mg/mL DNase I (Worthington, code# DP100). Cells were then passed through a 70 μm-strainer (Falcon, code# 352350) and then red blood cells were lysed in ammonium-chloride-potassium buffer. Samples were centrifuged at 300 xg at 4^{o}C for 5 minutes, supernatants were discarded, and pellets

were resuspended in PBS containing 2% FCS (FACS buffer) to establish single cell suspensions.

3.5 Flow cytometric analysis

A fraction (2 x 10^5) of cells recovered from tumors were stained with antibodies for 30 min at 4^{o}C in the dark. Antibodies used were: anti-B220 (eBioscience, clone RA3-6B2, code# 25-0452-82) for B cells; anti-Cd3 (eBioscience, clone 145-2C11, code# 17-0031-82), anti-Cd4 (eBiosciences, clone GK1.5, code# 25-0042-82), and anti-Cd8 (BioLegend, clone 53-6.7, code# 100707) for T cells; anti-Cd11b (BioLegend, clone M1/70, code# 101215), anti-Ly6c (BioLegend, clone HK1.4, code# 128005), and anti-Ly6g (BioLegend, clone RB6-8C5, code# 108411) for MMD and GMD respectively; anti F4/80 (eBiosciences, clone BM8, code# 17-4801-80) for TAM; and anti-Emmprin (BioLegend, clone OX-114, code# 123705), anti-Cd44 (eBiosciences, clone IM7, code# 11-0441-81), and anti-Cd133 (eBiosciences, clone 13A4, code# 12-1331-80) for LLC cells. Cells were then washed twice with FACS buffer, stained with 7AAD Viability Staining Solution, and analyzed on FACS Aria II or III (BD Biosciences). Flow cytometric data were analyzed using FlowJo software (Tree Star Inc.).

3.6 RNA extraction, cDNA synthesis and quantitative RT-PCR

Total RNAs were isolated from sorted or cultured cells using a RNeasy Mini Kit (Qiagen, code# 74106), and RNA quality was determined by an Agilent 2100 Bioanalyzer using an Agilent RNA 6000 Pico Chip (Agilent, code# 5067-1513). cDNAs were synthesized using SuperScript™ III Reverse Transcriptase (10,000 units; Invitrogen, code# 18080-044). cDNA quantity and quality were assessed using a Qubit 4 Fluorometer (Thermo Fisher Scientific) and a Qubit™ dsDNA HS Assay Kit (Invitrogene, code# Q32851), respectively. Primers and probes to determine expression levels of RNAs were TaqMan® Gene Expression Assays of Thermo Fisher Scientific Il1b (Mm00434228_m1), S100a8 (Mm00496696_g1), S100a9 (Mm00656925_m1), Vegfa (Mm00437306_m1), and TaqMan Ribosomal RNA Control Reagents for 18S ribosomal RNA (Thermo Fisher Scientific, code# 4308329). Quantitative RT-PCR (qPCR) was performed on a 7500 Real-Time PCR system (Applied Biosystems) using FastStart Universal Probe Master (Rox) (Roche, code# 38460200) according to manufacturer's instructions. Expression of targeted transcripts was normalized to that of *Rn18s*.

3.7 Whole transcriptome analysis (WTA)

$Cd11b^{+}Ly6g^{+}Ly6c^{-}$ granulocytic myeloid-derived cells (GMD), $Cd11b^{+}Ly6g^{-}Ly6c^{+}$ monocytic myeloid-derive cells (MMD), and $Cd11b^{+}Gr1^{-}F4/80^{+}$ TAM were sorted from

single cell suspensions prepared from tumors in *Tet2*$^{+/+}$ or *Tet2*$^{-/-}$ mice. Cells were sorted directly in RLT buffer of the RNeasy Mini Kit (Cat# 74106) and then total RNA was extracted. cDNA libraries were generated from total RNAs using a SMARTer Stranded Total RNA-Seq Kit v2-Pico Input Mammalian (Takara Bio USA Inc., code# 634412) and sequenced on a HiSeq X system (Illumina) with a standard 150-bp paired end read protocol.

LLC cells (the Cd45^{-}Cd44^{+}Cd113^{-} population) were also sorted from single cell suspensions described above and similarly subjected to WTA.

3.8 Reads alignment and differential expression analysis of WTA

After quality control procedures, sequencing reads were mapped on the mm10 mouse reference genome using the CLC Genomics Workbench ver.11 (Qiagen). The reads per kilobase of exon model per million mapped reads (RPKM) value was computed for each gene. The Differential Expression for WTA tool was used to perform a statistical differential expression test between *Tet2*$^{-/-}$ and *Tet2*$^{+/+}$ groups to identify examining differentially expressed genes (DEGs) between groups.

3.9 Pathway and functional annotation analyses

Gene set enrichment analysis (GSEA 4.1.0, https://www.gsea-msigdb.org/gsea/index.jsp) was applied to identify significantly enriched pathways in

each group. Gene sets from Molecular Signatures Database (MSigDB 7.1) were used for analysis. Metascape (https://metascape.org/gp/index.html#/main/step1) and DAVID Bioinformatics Resources 6.8 (https://david.ncifcrf.gov) were then applied for functional annotation of DEGs.

3.10 Single cell RNA sequencing (scRNA-seq) of $Cd45^+$ cells

$Cd45^+$ immune cells were sorted from $1x10^7$ cells prepared from tumors from *Tet2*$^{+/+}$ or *Tet2*$^{-/-}$ mice using MACS Anti-APC MicroBeads (Miltenyi Biotec, code# 130-090-855) and APC anti-mouse Cd45 antibody (Invitrogen, clone 104, code# 47-0454-80), according to manufacturer's instruction. Cells were then used to establish barcoded scRNA-seq libraries using Chromium Single Cell 3' Reagent kits (V2) (10X Genomics) according to the manufacturer's instructions (CG000183 Rev A), targeting 4,000 cells per library. Library quality control and quantification were performed using a 2100 Bioanalyzer High Sensitivity DNA kit (Agilent, 5067-4626) and a KAPA Library Quantification Kit (Kapa Biosystems, code# KK4824). Libraries were sequenced on the HiSeq X Ten system with a depth of 50,450 reads per cell for *Tet2*$^{+/+}$ and 82,634 for *Tet2*$^{-/-}$. Sequencing reads were mapped to the mouse genome (build GRCm38) and demultiplexed using Cell Ranger pipelines (10x Genomics, version 3.0.2).

3.11 Data processing, integration and cell clustering

Pre-processed data were further processed using R package *Seurat version 3.0 version* on RStudio (version 1.4). Genes related to ribosomes were removed. Cells with fewer than 200 unique feature counts, those with unique feature counts greater than 5000, and those with the number of mitochondrial genes > 5% were also removed. Data were normalized using the "NormalizeData" function and highly variable features were extracted using the "FindVariableFeatures" function. I then performed a linear transformation (scaling) and principal component analysis (PCA) based on variable features using the "RunPCA" function.

Canonical correlation analysis (CCA) [16] was performed to identify shared sources of variation across data of *Tet2*-deficient and WT $Cd45^{+}$ cells using the "FindIntegrationAnchors" function and integrate them using anchors using the "IntegrateData" function with canonical correlation dimensions of 20.

Graph-based clustering was then performed using "FindNeighbors" and "FindClusters" functions with the dimension of a reduction of 20, and resolution of 0.7. A non-linear dimensional reduction Uniform Manifold Approximation and Projection (UMAP) technique was used to visualize data using "RunUMAP" and "DimPlot" functions. Cell clusters were annotated based on expression of canonical markers,

including *Itgam*, *Gsr*, *Ly6g*, *Ly6c2* and *Adgre1* for GMD, MMD and TAM, *H2-Aa* and *H2-Eb1* for DC, *Cd3e* for Lympho T cells and *Cd79a* for Lympho B cells. The top 5 markers of each cluster were determined to identify novel markers either highly or uniquely expressed in each cluster.

3.12 DEG analysis

"FindMarkers" or "FindAllMarkers" functions were used to detect DEGs in each subcluster between *Tet2*-deficient and WT $Cd45^+$ cells, using the Wilcoxon Rank-Sum test and a minimum log fold-change in gene expression between *Tet2*-deficient and WT cells of 0.25. DEGs were defined as genes confirmed to show an adjusted p-value (based on the Bonferroni correction) of < 0.05.

3.13 Enzyme-linked immune sorbent assay (ELISA)

To collect plasma, blood was taken from the superficial temporal vein into tubes containing 3 μL 0.5 mM EDTA, which were then centrifuged at 1000 xg for 10 min at 4 °C. Plasmas were transferred into new tubes and stored at -80 °C to use. In vitro experiments, supernatants from cell culture were collected and then re-centrifuged at 300 xg for 10 min at 4 °C. Supernatants were transferred to new tubes, then kept at -80 °C until use or assayed within one day.

S100a8, S100a9, Il1b, and Vegf were detected using mouse ELISA Kits for S100a8 (Abcam, code# ab213886), S100a9 (Abcam, code# ab213887), Il1b (Abcam, code# ab197742), and Vegf (Abcam, code# Ab100751) based on the manufacturer's protocol. A human VEGF ELISA Kit (Abcam, code# 100662) was used to detect VEGF secreted from human lung cancer lines.

3.14 Proliferation assay

A Cell Counting Kit (CCK)-8 assay (Dojindo, code# CK04-05) was used to measure proliferation, based on the manufacturer's instructions. To do so, 1,000 LLC cells were seeded into each well of 96-well flat plates (Corning, code# 3959) and then treated with a dilution series of recombinant mouse S100a8/a9 heterodimeric protein (R&D, 8916-S8-050) at 0, 0.001, 0.003, 0.01, 0.04, 0.156, 0.625, and 2.5 μg/ml, with 3 replicates for each concentration. At indicated time points between 12 to 72 hours after treatment, 10 μL CCK-8 solution was added to each well, then, incubated at 37^{o}C for 2 hours and assayed using a Varioskan™ LUX multimode microplate reader (Thermo Fisher Scientific) at OD450.

3.15 Treatment of cancer cells in vitro

5 x10^{5} LLC cells in 12 well-plates were treated with or without 1 μg/ml recombinant mouse S100a8/a9 heterodimeric protein (R&D, 8916-S8-050). Supernatants were

collected after 24 hours to determine Vegf protein levels. In other experiments, 5 x10^5 human cancer cells (LC-Ad-1 and A549) were similarly treated and assayed for VEGF concentration.

To co-culture LLC cells with GMD, 5000 GMD were sorted from tumors of LLC-injected *Tet2*$^{+/+}$ or *Tet2*$^{-/-}$ mice and then cultured in wells of 96-well plates in which LLC cells had been previously cultured for 24 hours. Control wells contained only cultured LLC cells. After 24 hours, supernatants from all samples were collected to determine Vegfa protein levels. For anti-Emmprin antibody treatment, 1 hour after seeding GMD with LLC cells, an anti-Emmprin antibody (Cd147 monoclonal antibody functional grade; eBioscience, clone RL73, code# 16-1471-38) or isotype control (rat IgG2a kappa isotype control functional grade; eBioscience, clone BR2a, code# 16-4321-85) was added. After additional 24 hours, supernatants were collected to determine Vegfa protein levels.

3.16 Mouse antibody treatment

Tet2$^{-/-}$ or *Tet2*$^{+/+}$ mice were subcutaneously injected with 2 × 10^5 LLC cells in 100 μl PBS at the right flank. Tumor size was then measured by digital calipers and calculated as length x width x width x 0.52 every 2 days. Starting at day 8 after injection, the anti-Emmprin antibody (Cd147 monoclonal antibody functional grade; eBioscience, clone RL73, code# 16-1471-38) or isotype control (rat IgG2a kappa isotype control functional

grade; eBioscience, clone BR2a, code# 16-4321-85) was administered intraperitoneally at 10 μg in 100 μl PBS per mouse every 2 days with 4 does in total. Mice were analyzed at day 16. For treatment targeting to Il1b, at day 8 after injection, an anti-Il1b antibody (InVivoMAb anti-mouse/rat IL-1β, Bioxcell, code# BE0246) or isotype control (InVivoMAb polyclonal Armenian hamster IgG, Bioxcell, code# BE0091) was administered intraperitoneally at 50 μg in 100 μl PBS per mouse every 2 days with 4 doses in total. Mice were analyzed at day 16.

3.17 Immunohistochemical and immunofluorescence staining of tumor sections

Portions of tumors resected from LLC-injected *Tet2*$^{+/+}$ and *Tet2*$^{-/-}$ mice were fixed in 10% formalin for 24 hours at room temperature (RT) in 0.01 mol/L phosphate buffer (pH 7.2) and embedded in paraffin. Sections were stained with hematoxylin and eosin (HE) and photographed using a Keyence BZ X710 microscope (Keyence Corporation, Osaka, Japan). Other tumor portions were frozen in OCT compound (Sakura Finetek Japan Co.,code# 4583) in hexane (Wako, code# 082-00426), chilled on dry ice, and then stored at -80ºC. Five μm sections were sliced from OCT blocks at -12ºC on a cryostat.

For immunohistochemistry staining of blood vessels, specimens were fixed with 4% formaldehyde for 10 min at RT, and then endogenous peroxidase was blocked using fresh 3% H_2O_2 for 10 min at RT. Sections were stained by anti-Cd31 antibody (BD Biosciences,

code# 12-1331-80) (diluted 1:100) using a M.O.M. Immunodetection kit (Vector Laboratory, code# BMK 22-02) for 30 min at RT and then incubated with the working solution of Biotinylated Anti-rat IgG from the kit (diluted 1:100) for 30 min at RT. Sections were then incubated with HRP-SA (Vector Laboratory, SA-5704-100) for 30 min at RT prior to addition of DAB (Dako, code# K3468) to detect the signal. Finally, sections were washed 10 minutes in tap water, counterstained with HE, dehydrated, coverslipped and then read on a Keyence (BZ-X710) microscope. Each specimen was viewed in 5 fields at 20x magnification and Cd31-positive areas were detected automatically using BZ-X Analyzer Software from Keyence (BZ-X710).

For immunofluorescent staining, sections were incubated with primary antibodies for 90 minutes at RT. For Ly6g and Vegfa co-staining, anti-Ly6g (Thermo Fisher Scientific, code# 13-5931-85) (1:10) and anti-Vegfa (Abcam, code# ab46154) (1:100) antibodies were used. For Ly6g co-staining with S100a8, anti-S100a8 (Proteintech, code# 15792-1-AP) (1:200) and anti-Ly6g (eBioscience, code# 11-5931-82) (1:50) antibodies were used. For Ly6g co-staining with S100a9, anti-S100a9 (Proteintech, code# 14226-1-AP) (1:100) and anti-Ly6g (eBioscience, code# 11-5931-82) (1:100) antibodies were used. As secondary antibodies, goat anti-Rat IgG (H+L) Cross-Adsorbed Secondary Antibody, Alexa Fluor 488 (Thermo Fisher Scientific, code# A-11006) (1:1000) was used for Ly6g

(Thermo Fisher Scientific, code# 13-5931-85) and goat anti-Rabbit IgG (H+L) Cross-Adsorbed Secondary Antibody, Alexa Fluor 594 (Thermo Fisher Scientific, code# A-11072) (1:1000) was used for Vegfa, S100a8 and S100a9 at RT for 30 minutes. After incubation with DAPI (Vector laboratories, code# H-1200), sections were photographed using a Leica TCS SP8 confocal laser scanning microscope (Leica Microsystems, Wetzlar, Germany) within 24 hours.

3.18 Statistical analyses

Results are shown as mean ± SD. A two-tailed Student's t-test was calculated to compare two groups. Two-way ANOVA was used for 4 groups of Emmprin antibody treatment experiment. A p value < 0.05 was considered statistically significant.

4. RESULTS

4.1 *Tet2*-deficent myeloid cells promote lung cancer progression

To define the function of *TET2*-mutated immune cells in lung cancers, I subcutaneously transplanted LLC cells, which are mouse lung cancer cells, into the back of *Mx-Cre* [15] x *Tet2* conditional knockout (*Tet2*$^{-/-}$), in which *Tet2* gene is disrupted in all the hematopoietic cells [13] or control (*Tet2*$^{+/+}$) mice and observed tumor growth by measuring the tumor size every other day (Fig. 3A). Tumor growth was enhanced in *Tet2*$^{-/-}$ relative to *Tet2*$^{+/+}$ mice (day 8, 56.19 ± 39.90 mm^3 vs 12.29 ± 18.78 mm^3, $p = 0.016$; day 14, 467.12 ± 179.58 mm^3 vs 127.16 ± 59.08 mm^3, $p < 0.001$; day 16, 848.01 ± 290.50 mm^3 vs 245.17 ± 188.53 mm^3, $p < 0.001$) (Fig. 3B). Tumor weights as determined at day 16 were also heavier in *Tet2*$^{-/-}$ relative to *Tet2*$^{+/+}$ mice (0.573 ± 0.073 g vs 0.258 ± 0.060 g, $p = 0.002$) (Fig. 3C), and tumors were macroscopically larger (Fig. 3D).

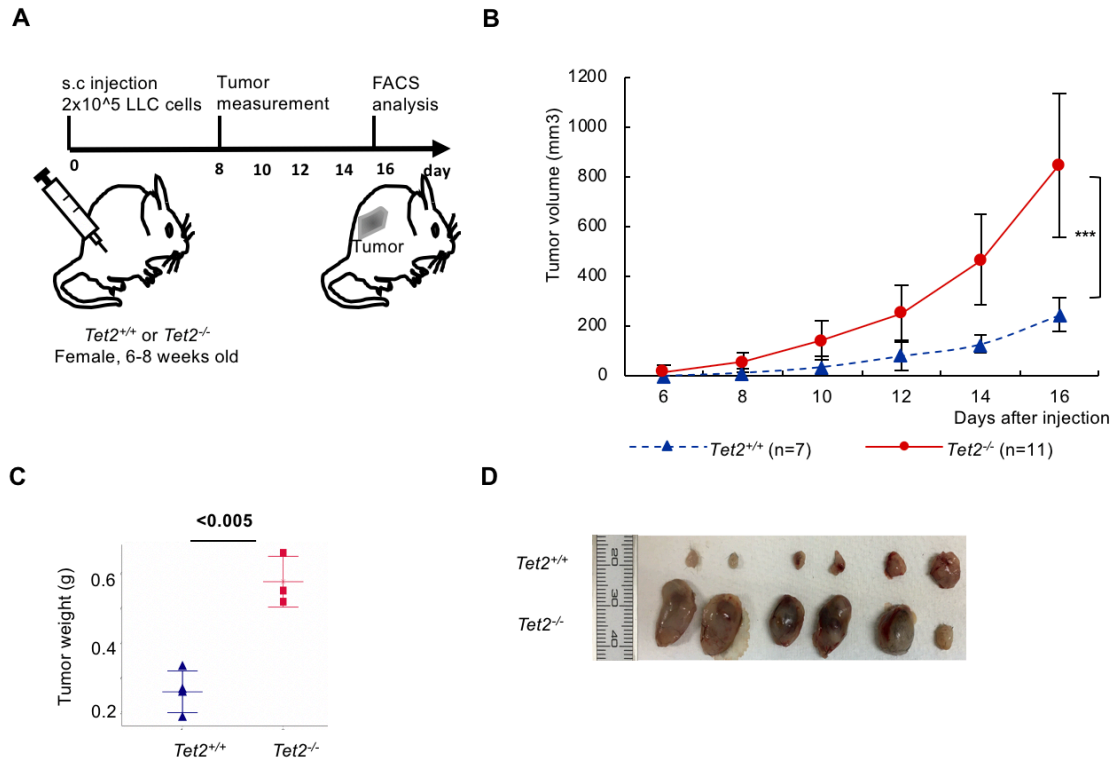

Figure 3. Tumor growth in *Tet2*$^{-/-}$ mice and WT.

(A) Experimental schema showing that 2x10^5 LLC cells were subcutaneously injected into flanks of *Tet2*$^{+/+}$ and *Tet2*$^{-/-}$ mice. (B) Tumor volume was measured every 2 days starting at day 8 (right). *Tet2*$^{+/+}$, n=7; *Tet2*$^{-/-}$, n=11. Mean ± s.d. is shown. (C) Weight of tumors at day16 after LLC injection. *Tet2*$^{+/+}$, n=4; *Tet2*$^{-/-}$, n=3. (D) Macroscopic analysis of tumors at day16 after LLC injection. *Tet2*$^{+/+}$, n=6; *Tet2*$^{-/-}$, n=6.

Based on flow cytometric analysis, immune cells from tumor tissues in both *Tet2*$^{-/-}$ and *Tet2*$^{+/+}$ mice primarily consisted of CD11b-positive myeloid cells (Figs. 4A, B). The proportion of GMD was slightly, but significantly, greater in tumor tissues from *Tet2*$^{-/-}$ compared to *Tet2*$^{+/+}$ mice, while that of MMD and TAM was comparable between

genotypes (*Tet2*$^{-/-}$ vs *Tet2*$^{+/+}$: GMD, 40.32% vs 24.68%, p = 0.018; MMD, 17.50% vs 22.00%, p = 0.291; TAM, 9.90% vs 9.86%, p = 0.964) (Fig. 4C).

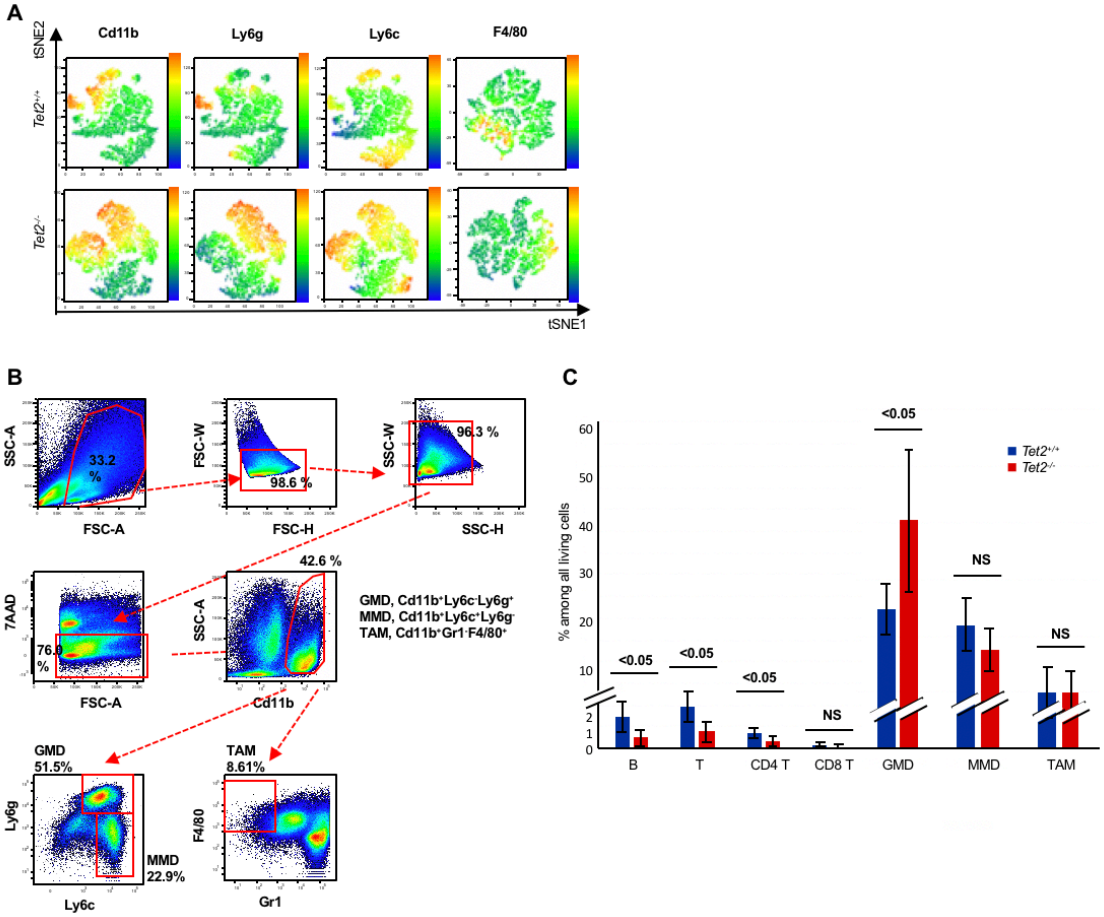

Figure 4. Flow cytometric data of immune cell fractions.

(A) Representative tSNE heatmaps of flow cytometric data. Shown are cell surface markers Cd11b, Ly6c, Ly6g and F4/80, which are markers used to define each myeloid lineage. (B) Illustration of gating strategy used to isolate myeloid populations in tumors. (C) The proportion of indicated immune cell subsets among living cells in tumors from *Tet2*$^{+/+}$ (n=7) and *Tet2*$^{-/-}$ (n=7) mice. For all panels, *p < 0.05; **p < 0.01; ns, not significant.

To further assess function of *Tet2*-deficient myeloid cells in lung cancer development, I then transplanted LLC cells in the back of $Tet2^{mye-/-}$ or $Tet2^{mye+/+}$ mice and observed tumor growth every other day (Fig. 5A, upper panel). Tumor growth was again enhanced in $Tet2^{mye-/-}$ relative to $Tet2^{mye+/+}$ mice (day 10, 32.59 mm^3 vs 4.21 mm^3, $p = 0.035$; day14, 238.97 mm^3 vs 33.96 mm^3, $p < 0.001$; day 16, 551.09 mm^3 vs 106.61 mm^3, $p < 0.001$) (Fig. 5A, lower panel). These data suggest that *Tet2*-deficient myeloid cells in the TME support tumor growth. Although the proportion of immune cells among living cells based on flow cytometric analysis was comparable in tumor tissues from $Tet2^{mye-/-}$ and $Tet2^{mye+/+}$ mice, the proportion of GMD in the $CD11b^+$ population was greater in $Tet2^{mye-/-}$ than in $Tet2^{mye+/+}$ mice, while MMD were decreased in $Tet2^{mye-/-}$ compared to $Tet2^{mye+/+}$ mice and TAM were comparable between these genotypes (Figs. 5B, C, D, E). These data suggest that *Tet2*-deficient GMD rather than MMD or TAM may play key roles in TME.

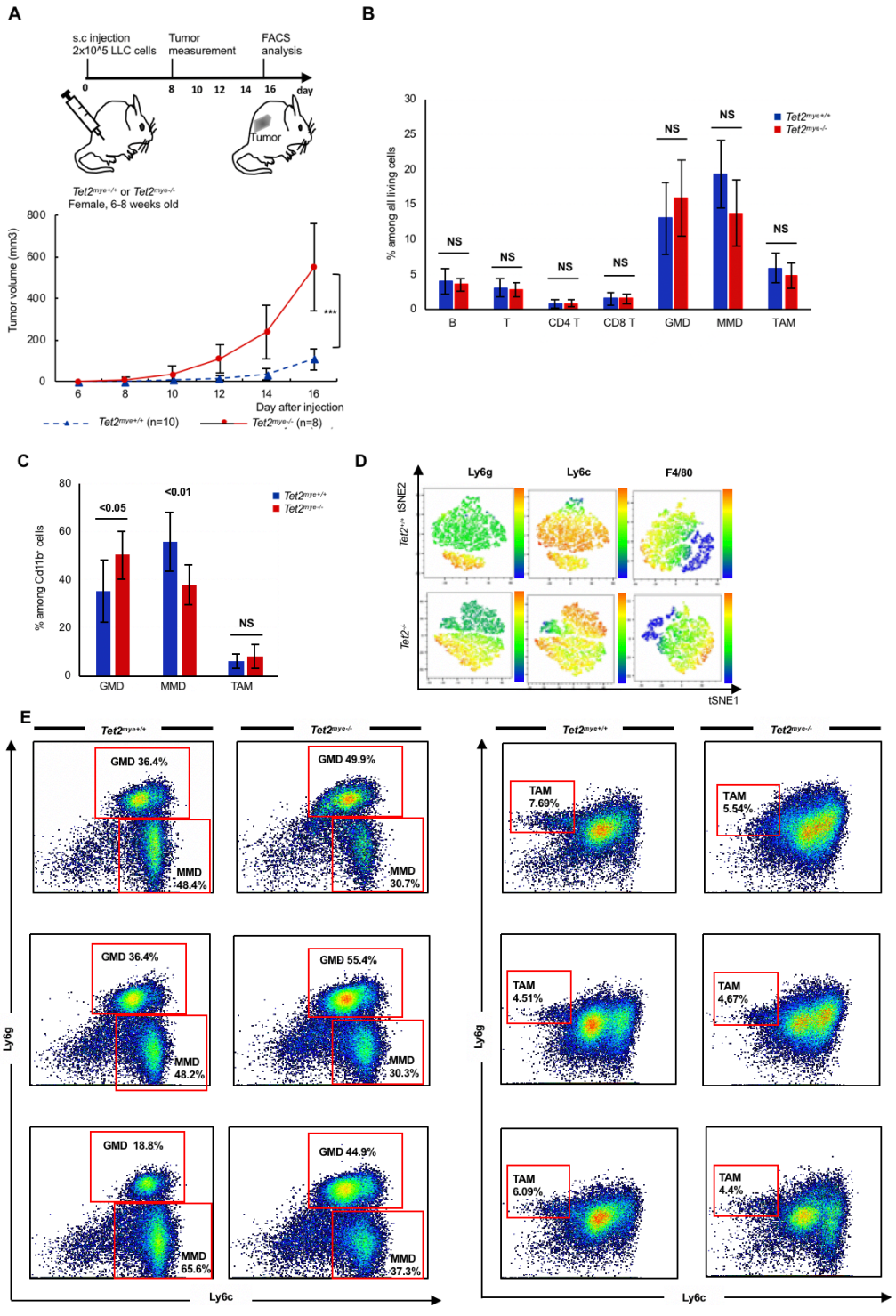

Figure 5. *Tet2*-deficient immune cells promote lung cancer progression in *Tet2*$^{mye-/-}$ mice and WT.

(A) Experimental schema showing that 2x10^5 LLC cells were subcutaneously injected into flanks of *Tet2*$^{mye+/+}$ and *Tet2*$^{mye-/-}$ mice (upper). Tumor volume was measured every 2 days starting at day 8.

Tet2$^{mye+/+}$ mice, n=10; *Tet2*$^{mye-/-}$ mice, n=8 (lower). Mean ± s.d. is shown. (B, C) Proportions of indicated immune cell subsets among living cells from tumors (B) and among CD11b^{+} subsets from tumors (C). *Tet2*$^{mye+/+}$, n=7; *Tet2*$^{mye-/-}$, n=8. (D) Representative tSNE heatmaps of flow cytometric data for Cd11b^{+} cell fractions from tumors in *Tet2*$^{mye+/+}$ and *Tet2*$^{mye-/-}$ mice. Markers of myeloid lineages are indicated. For all panels, *p < 0.05; **p < 0.01; ns, not significant. (E) Representative flow cytometry plots: percentages of GMD, MMD and TAM among Cd11b^{+} subsets from tumors. *Tet2*$^{mye+/+}$, n=3; *Tet2*$^{mye-/-}$, n=3.

4.2 Whole transcriptome analysis (WTA) identifies factors upregulated in *Tet2*-deficient myeloid cells that may support LLC cell growth

To identify candidate mediators from *Tet2*-deficent myeloid cells that support LLC cell growth, I first performed WTA of bulk RNAs extracted from GMD, MMD and TAM sorted from tumors in either *Tet2*$^{-/-}$ or *Tet2*$^{+/+}$ mice. Principal component analysis and unsupervised clustering revealed distinct gene expression patterns in each fraction between genotypes (Figs. 6A, B). When DEGs between *Tet2*-deficient and WT GMD, MMD and TAM, I observed the greatest changes in GMD, followed by TAM and MMD, revealing 130, 54, and 41 DEGs in each fraction between *Tet2*-deficient and WT groups, respectively (Fig. 6C).

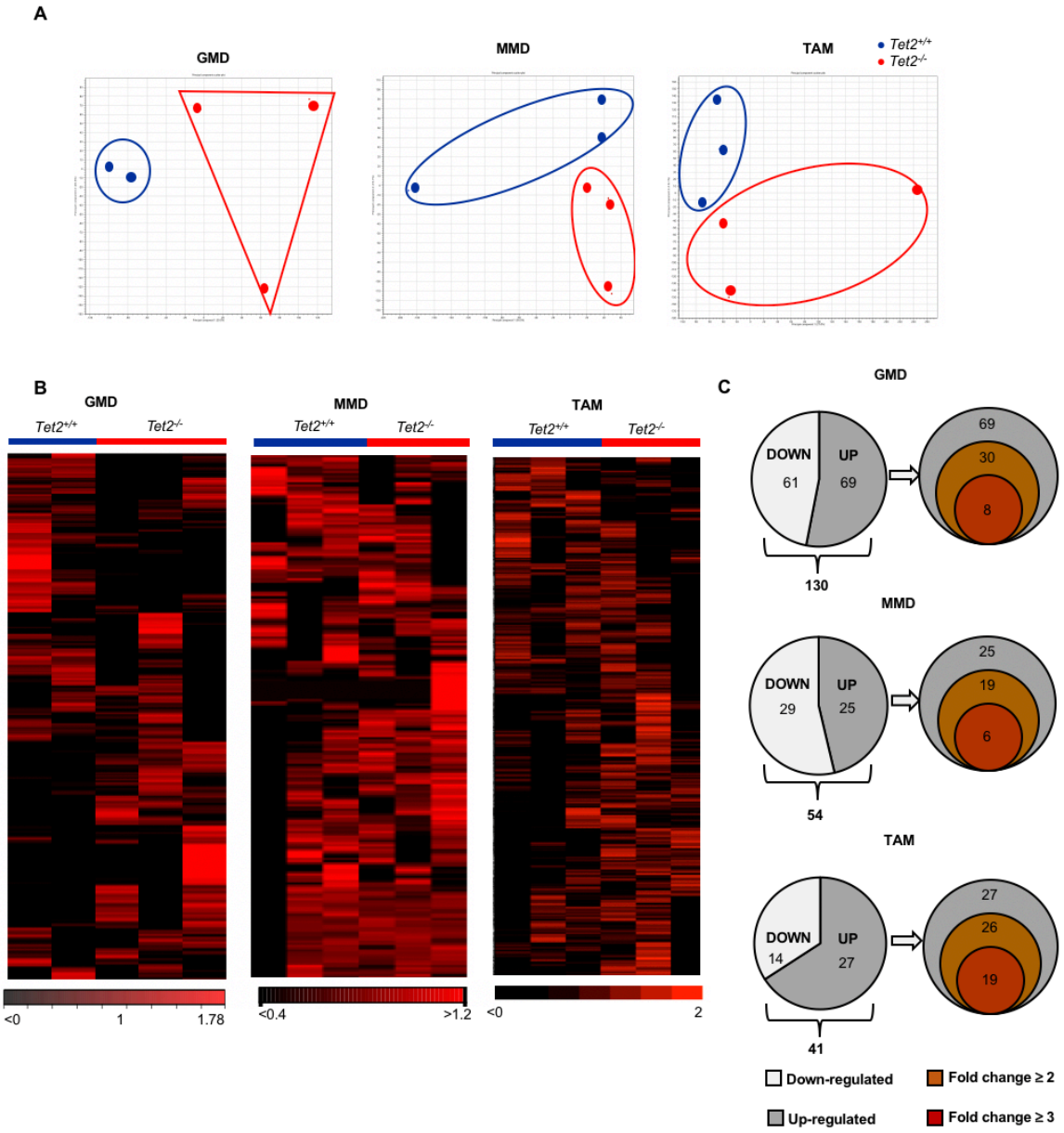

Figure 6. WTA of *Tet2*-deficient myeloid cells.

(A) PCA plots for WTA of *Tet2*-deficient and WT GMD, MMD and TAM. (B) Heatmaps of unsupervised clustering of genes differentially expressed in *Tet2*-deficient relative to WT GMD, MMD and TAM. Colors from black to bright red indicate gene expression from low to high; color scale shows log2 expression values. (C) Pie graphs showing the number of up- (grey) or down- (white) regulated genes with a FDR of

$p < 0.05$ for *Tet2*-deficient versus WT GMD, MMD and TAM (left column). Venn Diagrams show numbers of corresponding upregulated genes at various indicated fold-changes (right column).

To narrow my search, I identified genes highly expressed in the *Tet2*-deficient compared to WT group (FDR $p < 0.05$). Analysis of volcano plots and heatmaps indicated DEGs of each fraction upregulated in the *Tet2*-deficient compared to WT group with a fold-change >1.5 and FDR $p < 0.05$ (Figs. 7A, B). I then focused on 17 genes encoding secreted proteins from their gene ontology in DAVID analysis (https://david.ncifcrf.gov/) among a total of 113 genes upregulated in the *Tet2*-deficient group (Fig. 7C). Nine genes were extracted in the GMD, six in MMD, and four in TAM. In the GMD, S100a8 and S100a9 were among highly expressed genes in the *Tet2*-deficient relative to the WT group (Fig. 7C).

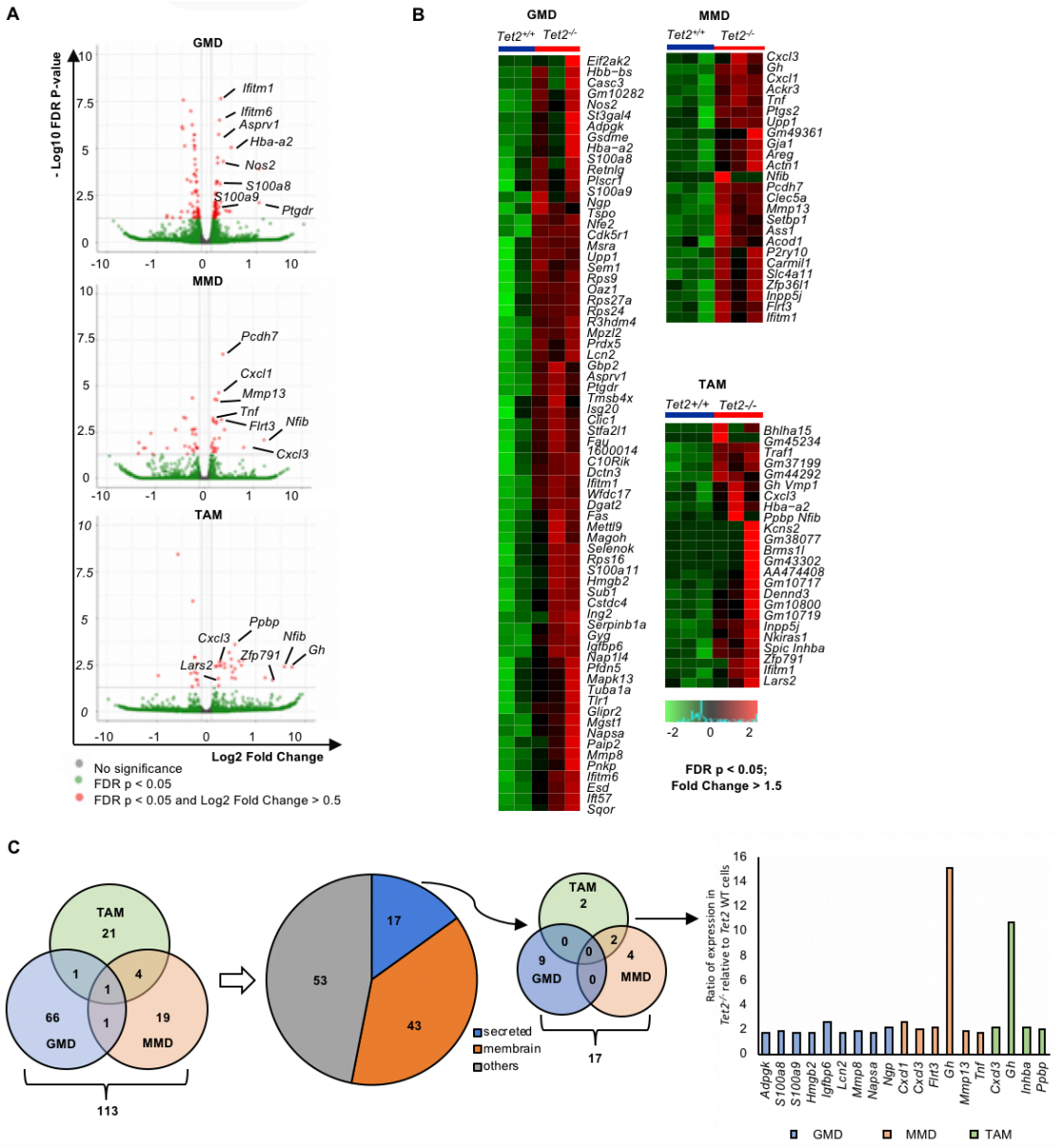

Figure 7. WTA of *Tet2*-deficient myeloid cells.

(A) Volcano plots showing DEGs from each fraction between *Tet2*-deficient and WT groups. (B) Heatmaps of supervised clustering of genes differentially expressed between *Tet2*-deficient and WT GMD, MMD and TAM. Genes upregulated in *Tet2*-deficient relative to WT groups are shown. Colors from green to red indicate FC from low to high. (C) Venn diagrams of genes up-regulated in GMD (69, light blue), MMD

(25, light orange) and TAM (27, light green). A total of 113 genes from GMD, MMD and TAM underwent DAVID analysis and were classified as encoding secreted proteins (blue), membrane proteins (orange) or others (grey). In the Venn diagram 17 genes encoding secreted proteins are distributed among indicated cell fractions. Bar chart shows gene list and ratio of expression in *Tet2*-deficient relative to WT cells.

4.3 Single-cell transcriptome analysis reveals immune-cell profiles and identifies candidate mediators that support tumor growth

To comprehensively define the immune-cell profiles and their transcriptome, I performed scRNA-seq analysis of Cd45-positive immune cells sorted from tumor tissues in $Tet2^{-/-}$ and $Tet2^{+/+}$ mice (Fig. 8A). After quality control procedures, I analyzed 4787 and 4000 immune cells from tumor tissues in $Tet2^{-/-}$ and $Tet2^{+/+}$ mice, respectively, and performed graph-based clustering to identify cell clusters. Subsequently each cell cluster was annotated using canonical markers (see methods). Three major myeloid components (GMD, MMD, and TAM), as well as DC, and lymphoid B and T cells accounted for 12.45%, 72.23%, 4.01%, 6.61%, 4.38%, and 0.32%, respectively (Figs. 8B-D). scRNA-seq analysis revealed a higher proportion of GMD among immune cells in tumor tissues

from *Tet2*$^{-/-}$ compared to *Tet2*$^{+/+}$ mice, in agreement with flow cytometric data (Fig. 8E).

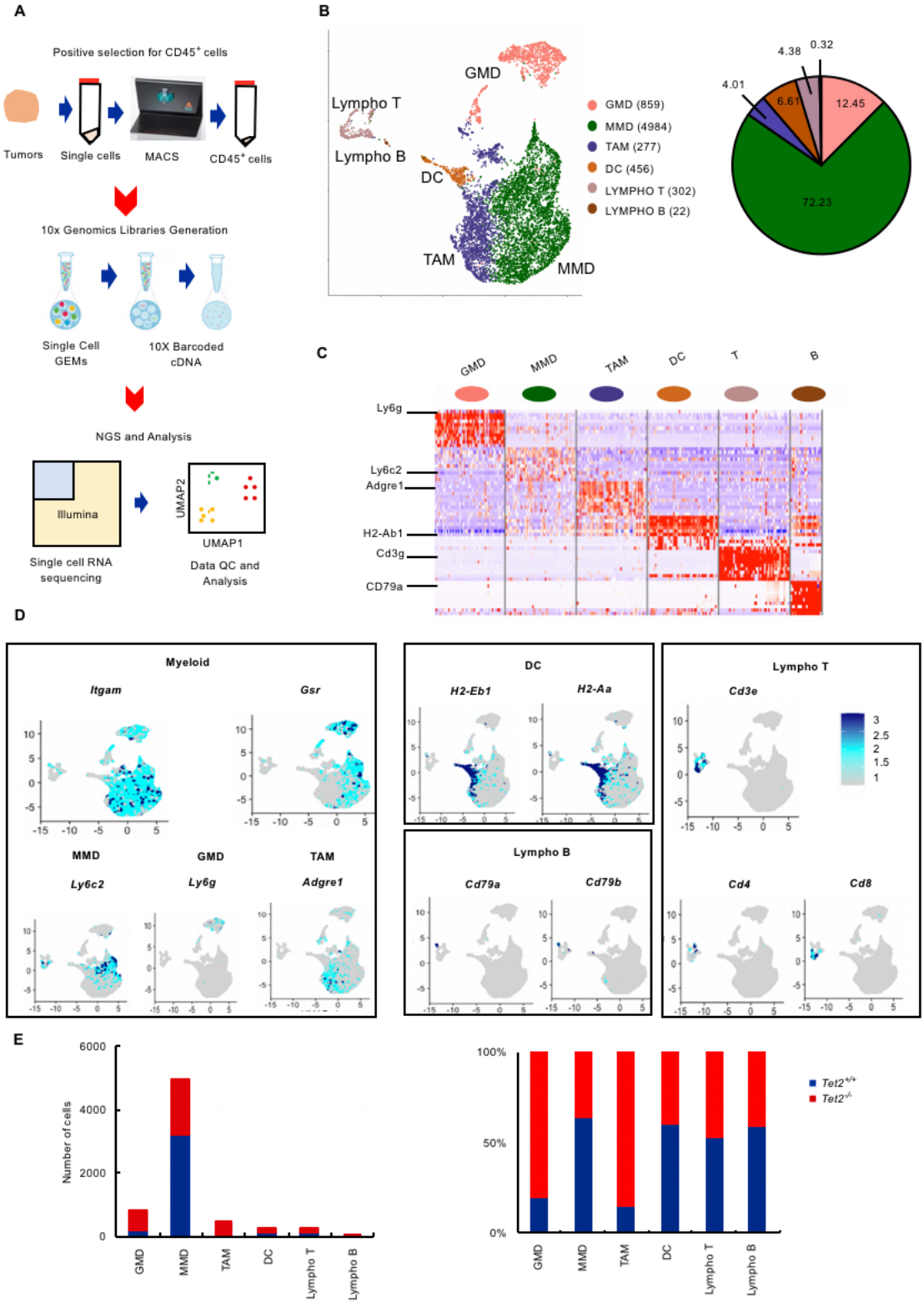

Figure 8. Flowchart of scRNA-seq to identify comprehensive immune-cell profiles and candidate growth mediators in *Tet2*-deficient GMD.

(A) Overview of workflow for scRNA-seq performed in this study. MACS, Magnetic-activated cell sorting; GEM, Gel Bead-in-Emulsion; NGS, next-generation sequencing; QC, Quality Control. (B) A UMAP plot after integration of *Tet2*-deficient and WT $Cd45^{+}$ immune cells from tumors (left). Six clusters corresponding to 6 cell types are labeled using different colors and the number of cells in each cluster is shown. Pie graph shows the proportion of cells in each cluster among total cells (right). (C) Heatmap of the top 10 conserved markers of each cell type. (D) Feature plots of common markers used to classify each cell type. Myeloid cells were divided into MMD, GMD and TAM by Itgam (Cd11b), Gsr (Gr1), Ly6c2, Ly6g and Adgre1 (F4/80). DC were identified by H2-Eb1 and H2-Aa (MHC-II markers), Lympho Ts by Cd3e, Cd4 and Cd8a, and Lympho Bs by Cd79a and Cd79b. (E) Bar charts indicate cell number (left) and proportions (right) of 6 cell types.

Notably, cell clusters were further divided into subclusters by unsupervised clustering: GMD into 3 (GMD1, GMD2, and GMD3), MMD into 5 (MMD1, MMD2, MMD3, MMD4, and MMD5), TAM into 4 (TAM1, TAM2, TAM3, and TAM4), and DC into 2 (DC1 and DC2) (Figs. 9A, B). Among all subclusters, the proportions of GMD1, GMD3, TAM3 and TAM4 were markedly higher in tumors from $Tet2^{-/-}$ than $Tet2^{+/+}$ mice (Figs. 9C, D).

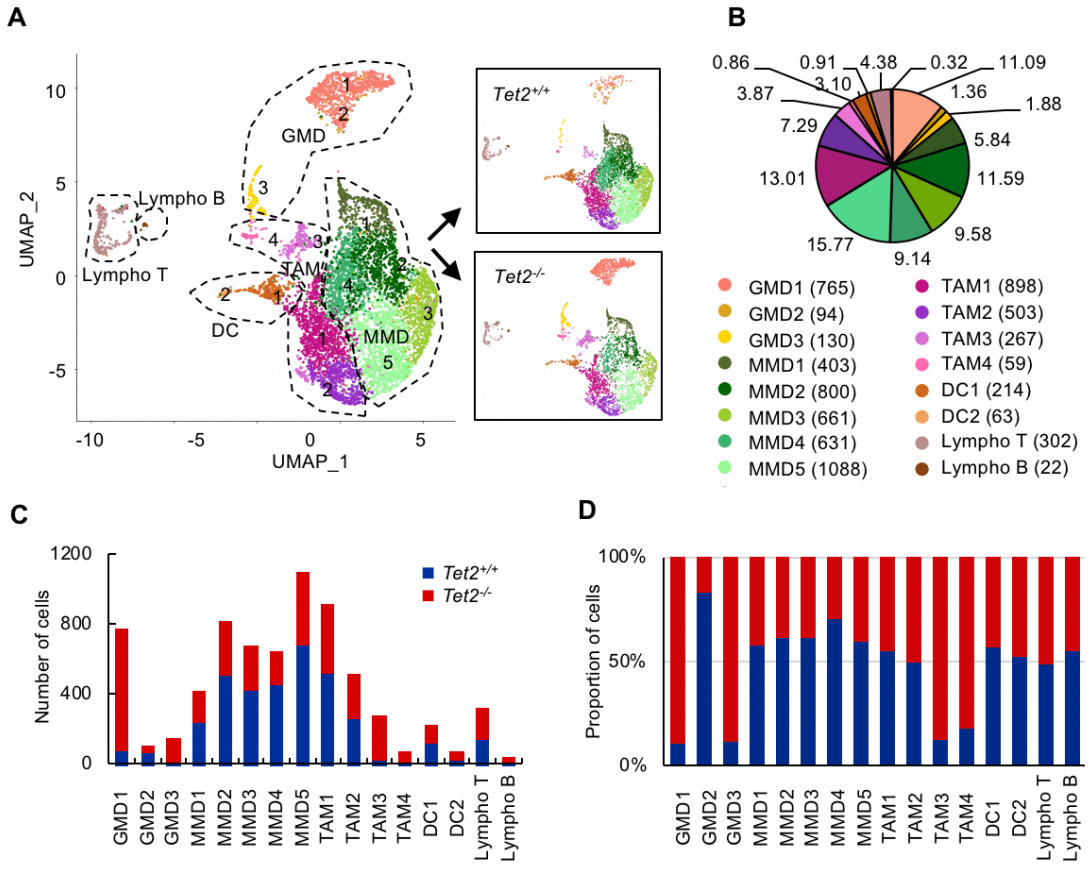

Figure 9. scRNA-seq reveals comprehensive immune-cell profiles.

(A) A UMAP plot after integration of *Tet2*-deficient and *Tet2*-WT Cd45^{+} immune cells from tumors (*Tet2*$^{-/-}$ vs *Tet2*$^{+/+}$, n=4787 vs n=4000). Sixteen clusters are labeled by different colors, while 6 cell types are indicated by dashed lines. (B) Pie graph shows proportion of cells in each cluster. (C, D) Bar charts indicate cell numbers (C) and proportions (D) in each cluster.

Table 1 lists the top 5 conserved markers for each subcluster. Notably, *S100a8* and *S100a9* were highly expressed in all GMD subclusters, but their levels were highest in GMD1 (Fig. 10A). MMD1, MMD2, MMD3, MMD4, and MMD5 were characterized by

high expression of *Adgre5*, *Itga1*, *Hspa1b*, *Cxcl10*, and *Gclm*, respectively (Fig. 10B). TAM1 and TAM4 specifically expressed *Clec12a* and *Hist1h1b*, respectively, while TAM2 and TAM3 exhibited high expression of *Cbr2* and *AY0361187*, respectively (Fig. 10B).

Table 1. The top 5 markers highly expressed in clusters of CD45 cells.

No.	Cluster	gene	p_val	avg_logFC	pct.1	pct.2	p_val_adj
1	GMD1	*S100a9*	0	3.6619474	1	0.61	0
2	GMD1	*S100a8*	0	3.6008872	0.988	0.559	0
3	GMD1	*Gm5483*	0	3.1815544	0.906	0.213	0
4	GMD1	*Retnlg*	7.50E-279	3.0239987	0.873	0.177	1.50E-275
5	GMD1	*Stfa2l1*	4.36E-117	2.809631	0.728	0.194	8.72E-114
6	GMD2	*S100a9*	1.68E-41	1.1820433	1	0.649	3.36E-38
7	GMD2	*S100a8*	2.66E-41	1.132321	1	0.601	5.31E-38
8	GMD2	*Hdc*	2.69E-39	0.8292277	0.989	0.476	5.39E-36
9	GMD2	*G0s2*	1.79E-33	0.9718507	0.819	0.3	3.57E-30
10	GMD2	*Cxcr2*	2.19E-33	0.8683871	0.851	0.326	4.38E-30
51	GMD3	*Cald1*	9.55E-86	2.7566731	0.969	0.259	1.91E-82
52	GMD3	*Gm26917*	2.27E-66	2.9794049	0.962	0.751	4.54E-63
53	GMD3	*Dst*	8.99E-64	2.4593517	0.931	0.555	1.80E-60
54	GMD3	*Hmga2*	3.62E-54	2.2739668	0.838	0.183	7.24E-51
55	GMD3	*Gm26870*	1.84E-10	2.6159146	0.654	0.334	3.69E-07
11	MMD1	*Gngt2*	2.33E-158	1.4121712	0.968	0.72	4.66E-155
12	MMD1	*Adgre5*	1.28E-122	1.0891883	0.839	0.383	2.55E-119
13	MMD1	*Hp*	7.89E-114	1.3351314	0.911	0.603	1.58E-110
14	MMD1	*Chil3*	2.13E-56	1.2319696	0.797	0.553	4.27E-53
15	MMD1	*Fn1*	1.52E-43	1.1886725	0.752	0.597	3.03E-40
16	MMD2	*Vcan*	8.74E-279	1.2098835	0.995	0.829	1.75E-275
17	MMD2	*Itga1*	3.71E-190	0.8937151	0.899	0.664	7.42E-187
18	MMD2	*Fn1*	4.64E-173	0.9650175	0.879	0.571	9.28E-170
19	MMD2	*Chil3*	5.73E-172	1.4652862	0.848	0.53	1.15E-168

20	MMD2	*Dmkn*	6.72E-159	1.0441625	0.824	0.549	1.34E-155
21	MMD3	*Ndrg1*	3.58E-175	1.1753423	0.946	0.795	7.15E-172
22	MMD3	*Hspa1a*	1.08E-138	1.7998893	0.859	0.625	2.16E-135
23	MMD3	*Hsp90aa1*	3.42E-119	1.263954	0.991	0.972	6.85E-116
24	MMD3	*Mt1*	2.32E-115	1.272976	0.949	0.845	4.64E-112
25	MMD3	*Hspa1b*	1.71E-112	1.7265782	0.781	0.516	3.43E-109
26	MMD4	*Mx1*	2.46E-271	1.5392613	0.949	0.637	4.92E-268
27	MMD4	*Ifit3*	3.84E-270	1.6833242	0.962	0.625	7.68E-267
28	MMD4	*Ifit2*	1.06E-248	1.6938069	0.924	0.607	2.12E-245
29	MMD4	*Rsad2*	4.58E-217	1.6653647	0.971	0.763	9.15E-214
30	MMD4	*Cxcl10*	9.14E-145	1.6644475	0.873	0.692	1.83E-141
31	MMD5	*Hmox1*	8.66E-222	1.2093445	0.989	0.901	1.73E-218
32	MMD5	*Prdx1*	1.88E-195	1.2748755	0.994	0.975	3.76E-192
33	MMD5	*Pf4*	7.99E-195	1.5547752	0.889	0.627	1.60E-191
34	MMD5	*Arg1*	1.72E-177	1.605917	0.806	0.569	3.44E-174
35	MMD5	*Ppbp*	1.37E-27	1.3871295	0.37	0.29	2.75E-24
36	TAM1	*C1qa*	4.44E-163	1.1936733	0.853	0.547	8.88E-160
37	TAM1	*C1qc*	1.24E-157	1.0529179	0.856	0.579	2.48E-154
38	TAM1	*C1qb*	4.16E-153	1.147579	0.888	0.708	8.32E-150
39	TAM1	*Ccl7*	2.38E-120	0.9833242	0.864	0.581	4.75E-117
40	TAM1	*Cxcl9*	3.70E-71	1.2126565	0.712	0.568	7.40E-68
41	TAM2	*C1qc*	1.88E-211	1.7674086	0.972	0.587	3.76E-208
42	TAM2	*C1qa*	2.69E-203	1.8822504	0.954	0.558	5.38E-200
43	TAM2	*Cbr2*	5.43E-201	1.5082011	0.871	0.241	1.09E-197
44	TAM2	*C1qb*	1.35E-195	1.6715207	0.978	0.712	2.70E-192
45	TAM2	*Ccl8*	5.33E-171	2.4783197	0.926	0.5	1.07E-167
46	TAM3	*Gm42418*	3.76E-108	1.9809251	1	1	7.52E-105
47	TAM3	*AY036118*	3.07E-63	1.4226547	0.918	0.946	6.14E-60
48	TAM3	*Acp5*	9.93E-10	1.0909412	0.326	0.242	1.99E-06
49	TAM3	*Hbb-bt*	3.50E-08	1.8543822	0.345	0.057	7.00E-05
50	TAM3	*Gm26917*	5.74E-06	1.5556694	0.715	0.757	0.01147014
56	TAM4	*Cpa3*	3.71E-34	2.4811262	0.407	0.051	7.41E-31
57	TAM4	*Top2a*	4.41E-24	2.12114	0.847	0.306	8.81E-21
58	TAM4	*Hist1h2ae*	7.80E-15	2.2044307	0.78	0.415	1.56E-11
59	TAM4	*Tpsb2*	5.62E-14	2.1689507	0.322	0.072	1.12E-10

60	TAM4	*Mcpt4*	0.0002674	2.8145358	0.339	0.086	0.53485904
61	DC1	*H2-Eb1*	1.83E-134	2.838175	1	0.574	3.66E-131
62	DC1	*H2-Aa*	2.17E-132	2.6786995	1	0.643	4.34E-129
63	DC1	*H2-Ab1*	5.38E-130	2.6663118	1	0.75	1.08E-126
64	DC1	*Cd74*	1.08E-127	2.1679369	1	0.828	2.15E-124
65	DC1	*Ifitm1*	3.93E-84	1.9601846	0.972	0.821	7.87E-81
66	DC2	*Ccr7*	3.35E-57	3.63565	1	0.273	6.70E-54
67	DC2	*Fscn1*	3.99E-56	3.0575661	0.952	0.155	7.99E-53
68	DC2	*Serpinb6b*	9.14E-55	3.1305203	0.984	0.275	1.83E-51
69	DC2	*Tbc1d4*	1.88E-52	3.4405529	1	0.275	3.77E-49
70	DC2	*Ccl5*	2.97E-41	3.3221448	0.984	0.446	5.93E-38
71	T	*Cd3g*	1.11E-278	2.8989607	0.987	0.138	2.22E-275
72	T	*Trbc2*	4.62E-268	3.1458226	0.987	0.227	9.24E-265
73	T	*Nkg7*	6.83E-216	3.2795426	0.97	0.326	1.37E-212
74	T	*Gzmb*	1.48E-184	3.0430756	0.911	0.302	2.96E-181
75	T	*Ccl5*	2.01E-136	2.8544928	0.897	0.43	4.01E-133
76	B	*Cd79a*	1.31E-81	2.7842508	0.909	0.035	2.63E-78
77	B	*Iglc3*	6.37E-50	2.5966944	0.909	0.086	1.27E-46
78	B	*Ebf1*	3.63E-47	2.8263811	0.955	0.095	7.26E-44
79	B	*Igkc*	4.59E-35	4.5551395	1	0.133	9.19E-32
80	B	*Ighm*	3.67E-17	2.7625069	1	0.489	7.34E-14

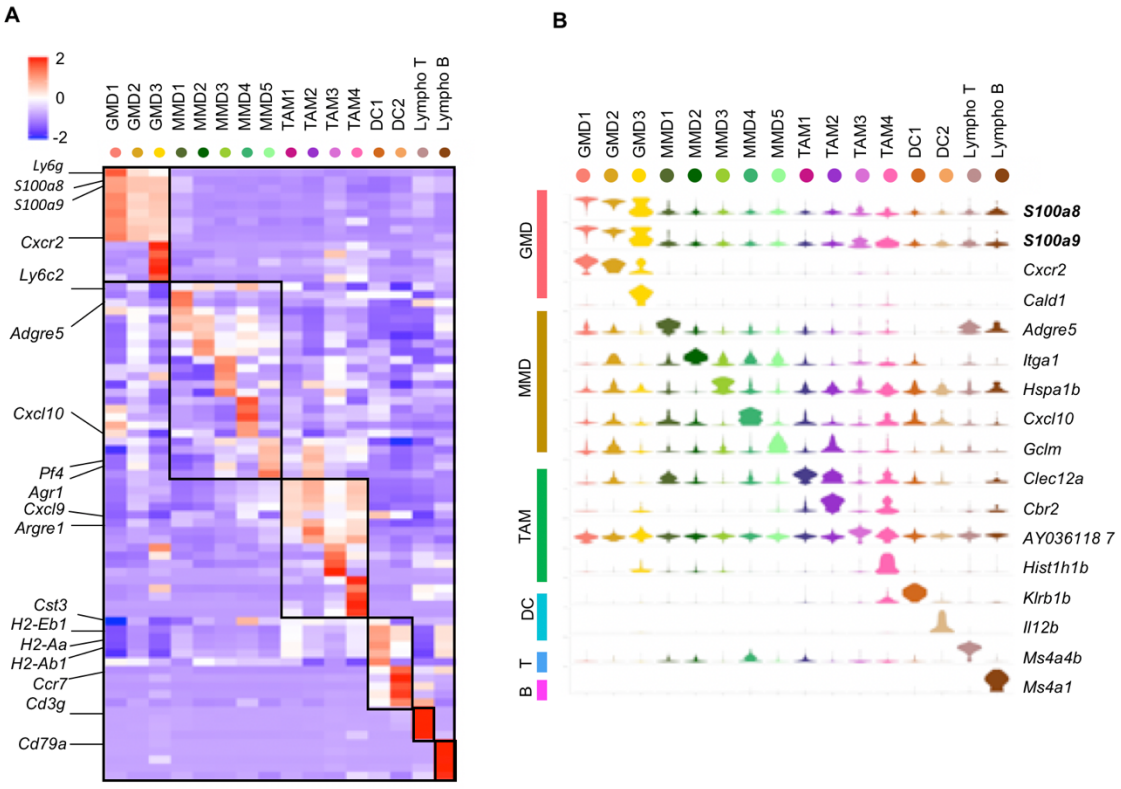

Figure 10. Single-cell transcriptome analysis reveals comprehensive immune-cell profiles.

(A) Heatmap of the top 5 conserved markers from each cluster indicated in (A). Rectangles are used to group clusters by cell type. (B) Stacked violin plots of conserved markers indicating their expression in indicated subclusters. Markers with either the highest or unique expression in each cluster are shown.

I then performed Metascape analysis to identify enrichment pathways for each subcluster. Remarkably, GMD1 expressed high levels of genes regulating tumor necrosis factor-activated receptor activity, secretion of cytokines involved in the immune response and interleukin (IL)-1 receptor activity (Table 2).

Table 2. The top 20 enrichment pathways in GMD1 of Cd45+cells based on scRNA-seq.

CLUSTER	GO	Description	LogP	Enrichment	Z-score
GMD1	R-MMU-6799990	Metal sequestration by antimicrobial proteins	-4.3	32	9.6
GMD1	GO:0050786	RAGE receptor binding	-6.1	24	11
GMD1	GO:0005031	tumor necrosis factor-activated receptor activity	-5	24	9.6
GMD1	GO:1904683	regulation of metalloendopeptidase activity	-3.6	21	7.7
GMD1	GO:0002374	cytokine secretion involved in immune response	-3.6	21	7.7
GMD1	GO:0070339	response to bacterial lipopeptide	-3.6	21	7.7
GMD1	GO:0035662	Toll-like receptor 4 binding	-3.6	21	7.7
GMD1	GO:1905049	negative regulation of metallopeptidase activity	-3.6	21	7.7
GMD1	GO:0071221	cellular response to bacterial lipopeptide	-3.6	21	7.7
GMD1	GO:0071220	cellular response to bacterial lipoprotein	-3.6	21	7.7
GMD1	GO:0070163	regulation of adiponectin secretion	-3.6	21	7.7
GMD1	GO:2000321	positive regulation of T-helper 17 cell differentiation	-3.6	21	7.7
GMD1	GO:0070162	adiponectin secretion	-3.6	21	7.7
GMD1	GO:0005035	death receptor activity	-4.5	19	8.3

GMD1	GO:2000562	negative regulation of CD4-positive, alpha-beta T cell proliferation	-4.5	19	8.3
GMD1	GO:0004908	interleukin-1 receptor activity	-3.4	18	7.1
GMD1	GO:0060613	fat pad development	-3.4	18	7.1
GMD1	GO:0008443	phosphofructokinase activity	-3.4	18	7.1
GMD1	GO:0033029	regulation of neutrophil apoptotic process	-4.3	17	7.9
GMD1	GO:0032493	response to bacterial lipoprotein	-3.2	16	6.6

I then analyzed DEGs for each subcluster between *Tet2*-deficient and WT immune cells. I observed the greatest changes in GMD1, followed by TAM1, MMD2, and MMD5 (Fig. 11A). Among DEGs observed in GMD1, *S100a8* and *S100a9* were highly expressed in the *Tet2*-deficient relative to WT group (Fig. 11B). Intriguingly, many DEGs, including *S100a8*, *S100a9*, *Cd14* and *Cxcl10,* were shared across various MMD and TAM subclusters including MMD1, MMD2, MMD3, MMD4, TAM1 and TAM2 (Figs. 11B, C). Metascape analysis of DEGs commonly upregulated in the *Tet2*-deficient group in multiple subclusters included leukocyte cell-cell adhesion, regulation of cytokine production, IL-17 signaling, and leukocyte migration (Fig. 11D). However, production of molecular mediators involved in immune and transcriptional dysregulation in cancer was a pathway specifically enriched in GMD1, whereas pathways related to blood vessel

endothelial cell migration and response to growth factor and vasculature development were enriched only in MMD and TAM subclusters (Fig. 11D).

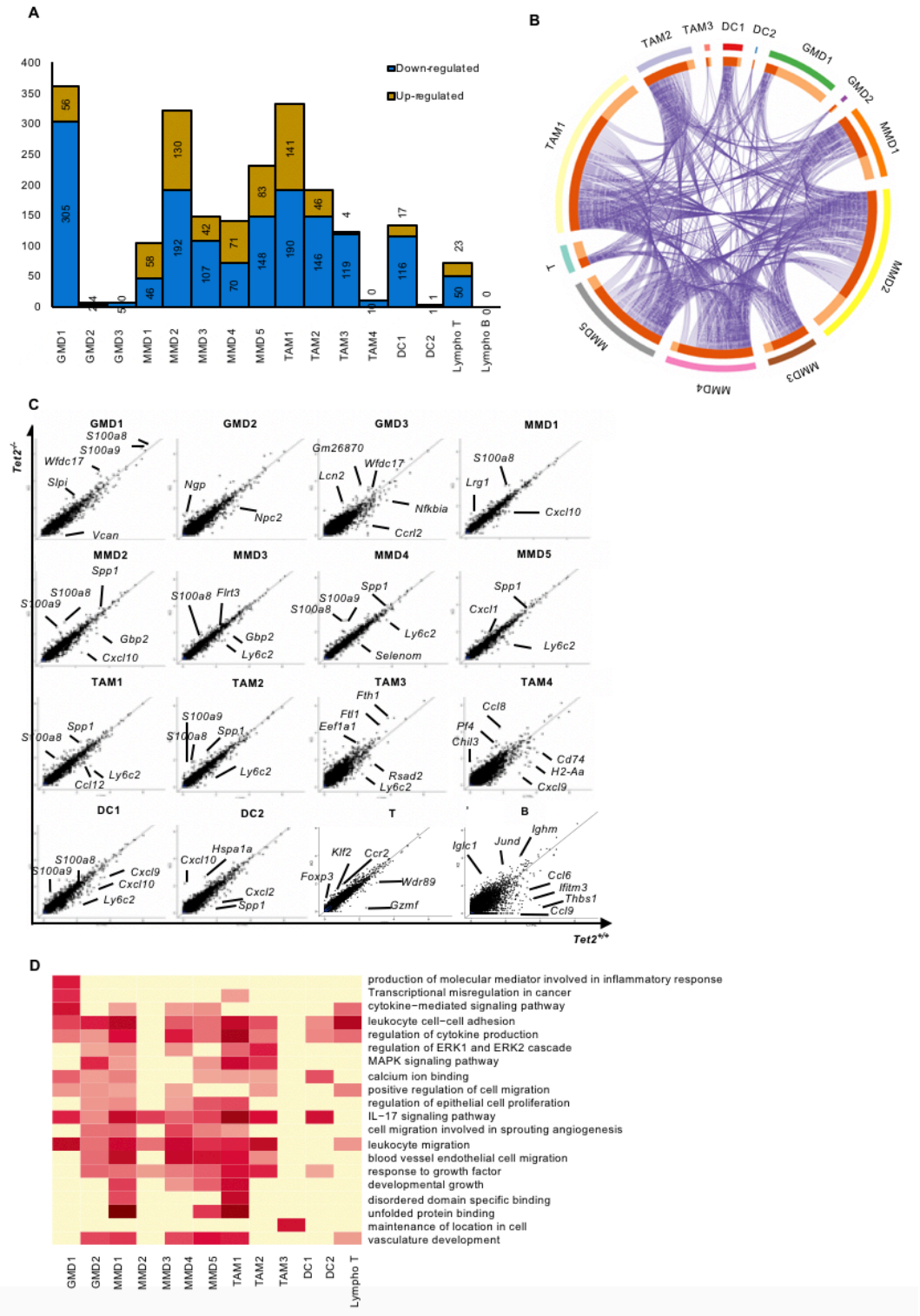

Figure 11. ScRNA-seq revealed comprehensive immune cell profiles.

(A) The number of DEGs in the indicated 16 clusters from *Tet2*-deficient immune cells relative to WT. Cut-off, adjusted P value < 0.05. (B) A circos plot from Metascape analysis indicates upregulated genes overlapping among the 13 clusters shown in (A). (GMD3, TAM4 and Lympho B were excluded due to lack of upregulated genes). (C) Scatter plots showing DEGs in each subcluster between *Tet2*-deficient and WT groups. (D) Metascape analysis showing the top 20 enrichment pathways of the 13 clusters described in (B). Cut-off, adjusted P value < 0.01.

Finally, after combining WTA and scRNA-seq data, I identified 39 genes commonly upregulated in the *Tet2*-deficient group. Seven of them, namely, *Ppbp, Igfbp6, S100a8, S100a9, Cxcl1*, *Flrt3,* and *Lcn2,* encode secreted proteins (Figs. 12A-D). *S100a8* and *S100a9* showed the greatest difference in *Tet2*-deficient versus WT groups (Figs. 12C, D). Thus, in this analysis I focused on *S100a8/S100a9* as candidate mediators.

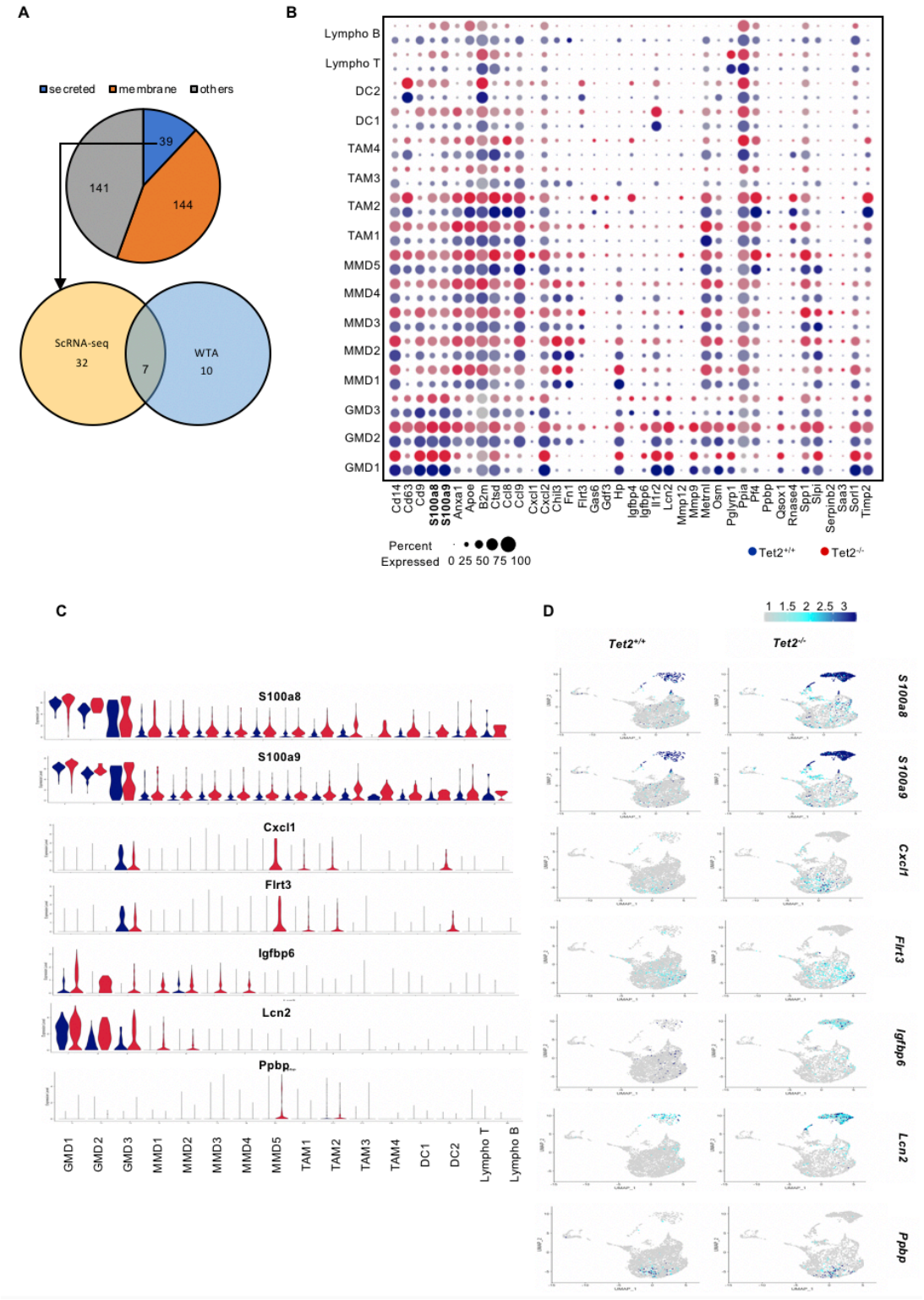

Figure 12. ScRNA-seq revealed comprehensive immune cell profiles.

(A) Pie graph (top) including 324 up-regulated markers from the 13 clusters described in Fig. 4.9B. David analysis was performed to narrow them to 39 genes that encoded secreted proteins (blue), 144 that encoded membrane proteins (orange), and 141 others (grey). The Venn diagram (bottom) shows the inter-relationship between scRNA-seq and WTA data from GMD, MMD and TAM for genes encoding secreted proteins, with 7 shared genes, and 32 and 17 specific genes to either scRNA-seq and WTA, respectively. (B) A dot plot of 39 genes of scRNA-seq selected in (A). Cut-off, adjusted P value < 0.05. Dot size and color indicate the percentage of cells and expression level in each subcluster, respectively. (C, D) Wrap Plots (C) and Feature Plots (D) of 7 genes from (A) shared by scRNA-seq and WTA.

4.4 S100a8/S100a9 proteins are present at higher levels in plasma of tumor-bearing *Tet2*$^{-/-}$ relative to *Tet2*$^{+/+}$ mice

I then sorted GMD from tumors from *Tet2*$^{+/+}$ and *Tet2*$^{-/-}$ mice to assess *S100a8* and *S100a9* mRNA expression by qPCR. Consistently, expression levels of both genes were higher in *Tet2*-deficient than in WT GMD ($p < 0.05$) (Fig. 13A). I then evaluated S100a8 and S100a9 protein levels in plasma of *Tet2*$^{-/-}$ and *Tet2*$^{+/+}$ mice, with or without tumors. Notably, S100a8 and S100a9 protein levels were higher in the tumor-bearing mice than the non-tumor-bearing mice ($p<0.005$) (Fig. 13B). In the tumor-bearing mice, S100a8 and S100a9 protein levels were significantly higher in *Tet2*$^{-/-}$ than in *Tet2*$^{+/+}$ mice ($p < 0.05$), while in non-tumor-bearing mice, levels were not significantly different between both

genotypes (Fig. 13B). These observations suggest that S100a8/S100a9 secreted from *Tet2*-deficient GMD may play essential roles in LLC growth in *Tet2*$^{-/-}$ mice.

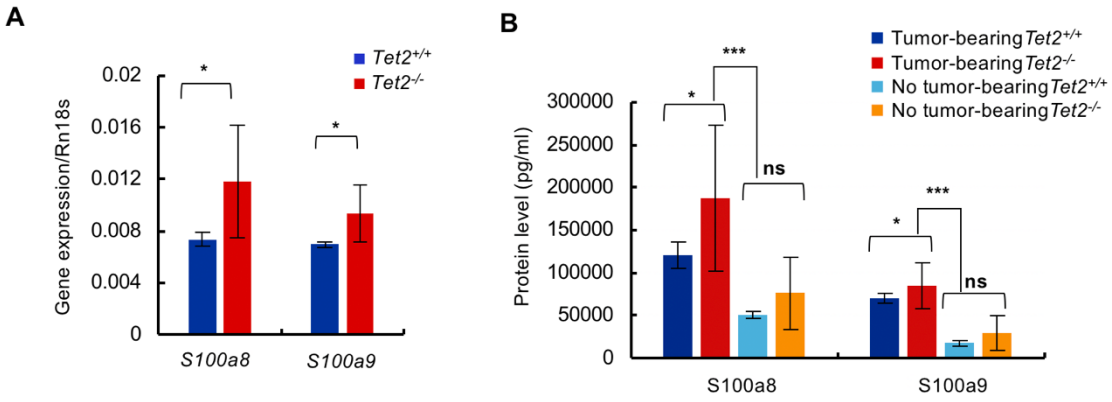

Figure 13. Expression of *S100a8* or *S100a9* transcripts in GMD and S100a8 and S100a9 protein levels in plasmas.

(A) Expression of *S100a8* or *S100a9* transcripts normalized to ribosomal *18s* (*Rn18s*) in GMD sorted from tumors in *Tet2*$^{-/-}$ (n = 3) and *Tet2*$^{+/+}$ (n = 4) mice. (B) S100a8 and S100a9 protein levels in plasma of either tumor-bearing or non-tumor-bearing mice, based on an ELISA assay. For each group, n = 3.

4.5 Treatment of *Tet2*$^{-/-}$ mice with anti-Emmprin antibody decreases tumor size

To further assess S100a8/S100a9 activity in tumor-bearing *Tet2*$^{-/-}$ mice, I first assessed expression of the S100a8/S100a9 receptor on LLC cells. Emmprin (Bsg/Cd147) as well as toll-like receptor 4 (Tlr4) and the receptor for advanced glycosylation end products (RAGE) (Ager) reportedly serve as S100a8/S00a9 receptors [17, 18]. Re-analysis

of WTA data from LLC cells [19] revealed high *Emmprin* expression in LLC cells, while *Ager* and *Tlr4* expression levels were very low (Table 3).

Table 3. FPKM values of S100a8/S100a9 and corresponding receptors.

Gene name	LLC-in vitro 1	LLC-in vitro 2	LLC-in vitro 3	LLC-in vitro 4	LLC-in vitro 5	LLC-in vivo 1	LLC-in vivo 2	LLC-in vivo 3	LLC-in vivo 4	LLC-in vivo 5
S100a8	0.01	1.08	0.01	0.48	0.14	5.83	0.80	1.96	3.02	5.20
S100a9	0.01	0.01	0.01	0.01	0.01	2.97	0.42	1.40	2.04	4.14
Tlr4	17.85	28.66	16.44	45.47	35.91	7.07	9.61	8.83	9.60	12.48
Bsg	216.75	526.04	262.27	568.81	453.19	500.37	287.38	281.49	398.37	328.44
Ager	0.56	0.12	0.80	0.62	0.29	0.56	1.09	2.55	0.54	0.69

I then confirmed Emmprin expression by flow cytometry on LLC cells maintained in vitro as well as those purified from tumors in $Tet2^{-/-}$ and $Tet2^{+/+}$ mice (Figs. 14A, B). Emmprin expression levels were slightly, but statistically higher in LLC cells recovered from tumors on a $Tet2^{-/-}$ than on a $Tet2^{+/+}$ background (Fig. 14B). I then tested the effect in vivo of administration of an anti-Emmprin neutralizing antibody to $Tet2^{-/-}$ or $Tet2^{+/+}$ mice that had been inoculated 8 days before with LLC cells (Fig. 14C). In $Tet2^{-/-}$ as well as $Tet2^{+/+}$ mice administration of anti-Emmprin antibody decreased the size of LLC tumors relative to mice administered isotype control (anti-Emmprin-treated $Tet2^{-/-}$ vs isotype-treated $Tet2^{-/-}$: day 16, 281.07 ± 153.49 mm^3 vs 1386.30 ± 137.60 mm^3, $p < 0.001$; anti-Emmprin-treated $Tet2^{+/+}$ vs isotype-treated $Tet2^{+/+}$: day 16, 110.92 ± 80.00 mm^3 vs 329.45 ± 19.16 mm^3, $p < 0.01$) (Figs. 14D-F). As a result, after the anti-Emmprin antibody

treatment, the tumor size was comparable between these genotypes. These data indicate that the blockade of S100a8/S100a9-Emmprin signaling is an effective treatment for tumors generated in immune cells with *Tet2* deletion.

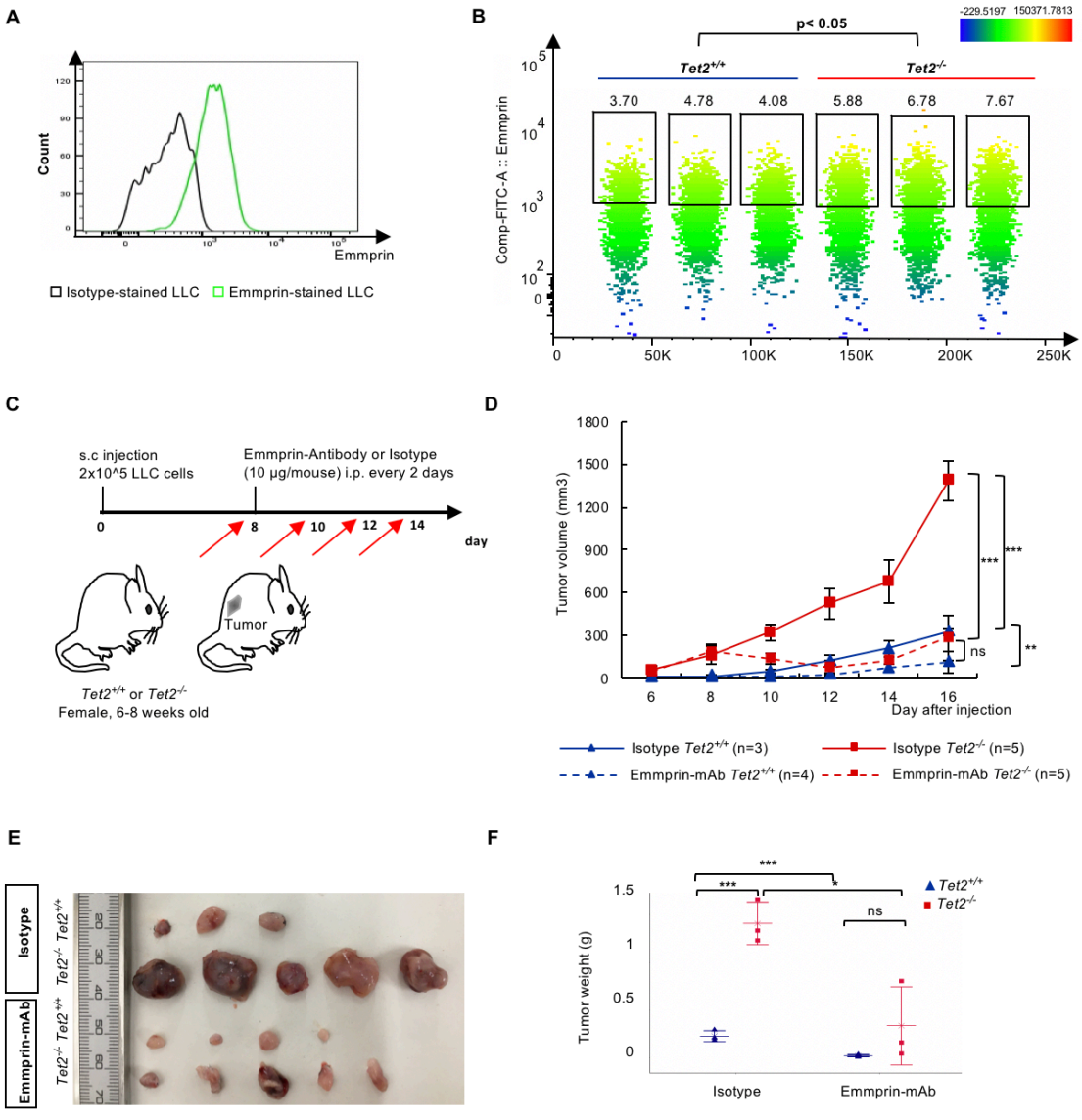

Figure 14. Administration of anti-Emmprin antibody.

(A) Histogram showing cell surface Emmprin protein expression in LLC cells. (B) A tSNE plot of flow cytometric data based on Emmprin expression on LLC cells extracted from tumors in *Tet2*$^{-/-}$ and *Tet2*$^{+/+}$ mice. *Tet2*$^{-/-}$, n=3; *Tet2*$^{+/+}$, n = 3. (C) Schematic showing time-line of injection of anti-Emmprin antibody or isotype control into *Tet2*$^{-/-}$ or *Tet2*$^{+/+}$ mice harboring LLC cell tumors. Red arrows indicate the timing when we inject either anti-Emmprin antibody or isotype. (D) Tumor volume was measured by digital calipers and calculated as length x width x width x 0.52 after subcutaneous LLC cell injection into flanks of indicated mice after treatment with either anti-Emmprin antibody or its isotype control. Mean ± s.d. is shown. (E, F) Macroscopic analysis (E) and tumor weight (F) of groups shown in (F) at day 16. For all panels, *p < 0.05; **p < 0.01; ***p < 0.005; ns, not significant.

4.6 Pathway analysis reveals that Il1b is a candidate upstream regulator of S100a8/S100a9 signaling

To define factors that might regulate *S100a8/S100a9* in GMD cells, I performed Ingenuity Pathway Analysis using DEGs ($p < 0.05$) from WTA of GMD. That analysis revealed that signaling of Il1b, a proinflammatory cytokine, could be upstream of S100a8/S100a9 activity (Fig. 15A). RNA-seq data revealed that *Il1b* mRNA expression was significantly increased in *Tet2*-deficient relative to WT GMD and MMD (Fig. 15B). GSEA also showed that 6 pathways related to *Il1b* were enriched in *Tet2*-deficient compared to WT groups (Figs. 15C, D). Gene ontology analysis of DEGs from WTA of

GMD, MMD and TAM revealed that the pathway "cellular response to IL-1" was among the top 10 common enriched pathways, even from DEGs derived from scRNA-seq of $Cd45^{+}$ cells (Fig. 15E and Table 4). qPCR analysis confirmed that *Il1b* mRNA expression was higher in *Tet2*-deficient GMD than in WT GMD (Fig. 15F). Il1b protein levels in plasma were also higher in $Tet2^{-/-}$ than in $Tet2^{+/+}$ mice (Fig. 15G).

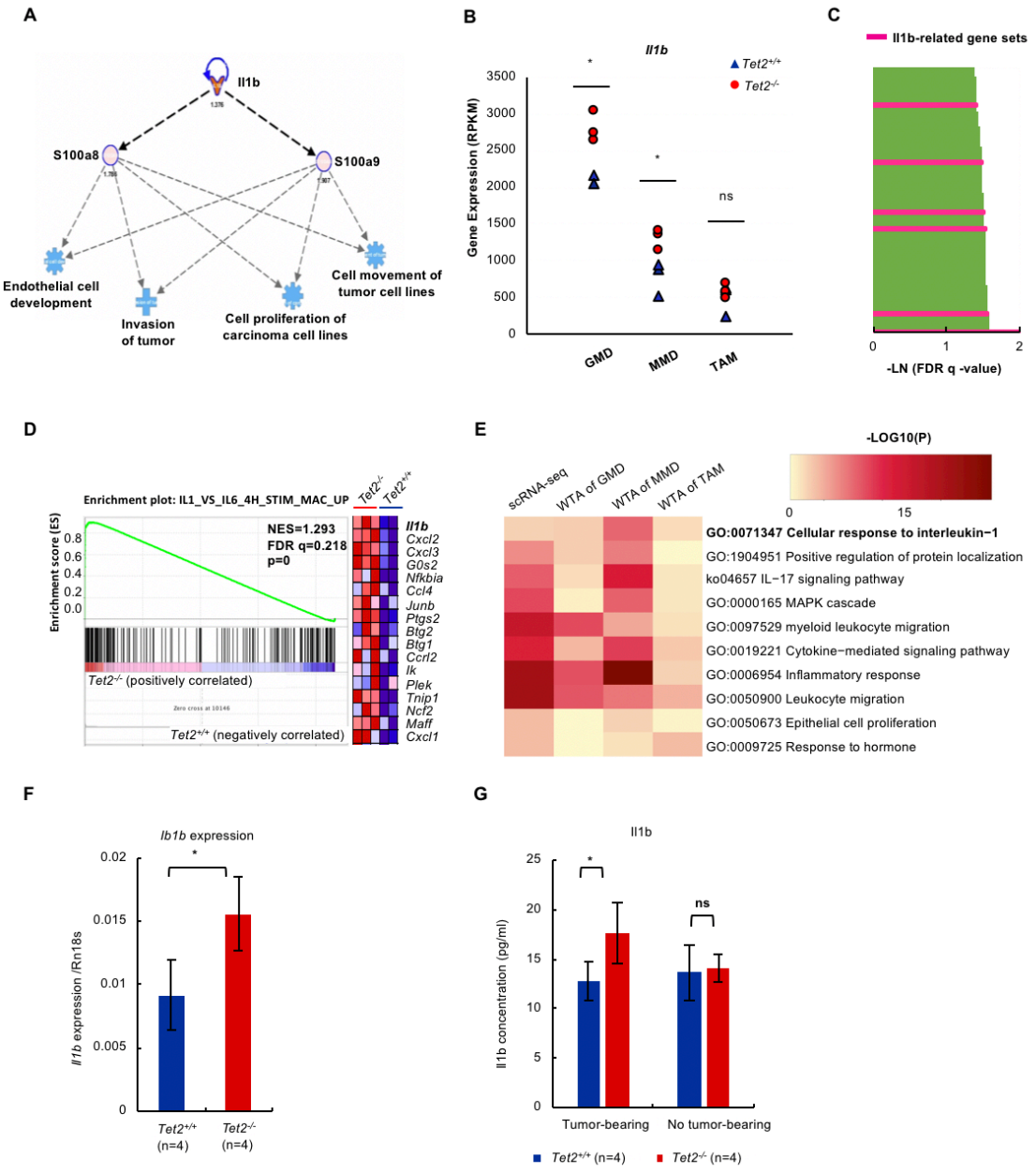

Figure 15. Pathway analysis revealing Il1b as a candidate regulator of S100a8/S100a9 signaling.

(A) Ingenuity pathway analysis of DEGs in GMD (cut-off, $p < 0.05$) to assess signaling upstream and downstream of S100a8 and S100a9. Il1b was identified as a candidate upstream factor. Four predicted downstream pathways are shown in blue. (B) Reads Per Kilobase of transcript, per Million mapped reads

(RPKM) values of *Il1b* from WTA data in either *Tet2*-deficient or WT GMD, MMD and TAM. (C) Gene sets enriched in *Tet2*-deficient relative to WT groups for WTA data from GMD. Pink bars, Il1b-related gene sets (cut-off; FDR $q < 0.25$, nominal $p < 0.05$). (D) Enrichment plot and heatmap of one enriched pathway related to *Il1b*, namely, the IL1_VS_IL6_4H_STIM_MAC_UP pathway, using WTA data from GMD. (E) Metascape analysis revealing the top 10 enrichment pathways as determined from upregulated gene sets of scRNA-seq data and WTA of GMD, MMD, and TAM. (F) *Il1b* mRNA expression normalized to *Rn18s* in GMD sorted from tumors from $Tet2^{-/-}$ (n = 3) and $Tet2^{+/+}$ (n = 4) mice. (G) Il1b protein levels in plasma of either tumor-bearing or non-tumor-bearing mice, based on ELISA. Each group, n = 4.

Table 4. Top 10 significantly enriched pathways from GO and KEGG enrichment analysis of scRNA-seq data and WTA data of GMD, MMD and TAM.

GO	Description	_LogP_CD45scRNAseq	_LogP_mRNAseq-GMD	_LogP_mRNAseq-MMD	_LogP_mRNAseq-TAM
GO:0071347	cellular response to interleukin-1	-3.6292191	-3.6924162	-7.6439643	-3.2133256
GO:1904951	positive regulation of establishment of protein localization	-6.1902007	-3.8007701	-6.7694037	-2.1373743
ko04657	IL-17 signaling pathway	-7.9299785	-3.2933656	-10.99263	-2.8586514

GO:0000165	MAPK cascade	-8.7034568	-2.5237574	-7.7411943	-2.8670897
GO:0097529	myeloid leukocyte migration	-12.53702	-8.6046712	-5.1965013	-3.0926284
GO:0019221	cytokine-mediated signaling pathway	-10.835677	-4.7070109	-9.1717688	-3.8588184
GO:0006954	inflammatory response	-15.606855	-8.4392808	-19.346601	-3.5283674
GO:0050900	leukocyte migration	-16.03232	-8.2135698	-7.0066308	-4.8721725
GO:0050673	epithelial cell proliferation	-4.3945533	-2.1704342	-3.5826776	-2.4066515
GO:0009725	response to hormone	-4.4851442	-2.2287992	-3.0013683	-4.4607612

To further assess the activity of Il1b-S100a8/S100a9 signaling in LLC development, I then tested the in vivo effect of an anti-Il1b neutralizing antibody to *Tet2*$^{-/-}$ or *Tet2*$^{+/+}$ mice that had been inoculated 8 days before with LLC cells (Fig. 16A). In *Tet2*$^{-/-}$ as well as *Tet2*$^{+/+}$ mice administration of the anti-Il1b antibody decreased the size of LLC tumors relative to mice administered isotype control (anti-Il1b-treated *Tet2*$^{-/-}$ vs isotype-treated *Tet2*$^{-/-}$: day 16, 217.02 ± 253.58 mm^3 vs 1414.92 ± 268.90 mm^3, $p < 0.005$; anti-Il1b-treated *Tet2*$^{+/+}$ vs isotype-treated *Tet2*$^{+/+}$: day 16, 19.50 ± 39.00 mm^3 vs 877.86 ± 110.23 mm^3, $p < 0.005$) (Figs. 16A-C). As a result, after the anti-Il1b antibody treatment, the tumor size was comparable between these genotypes.

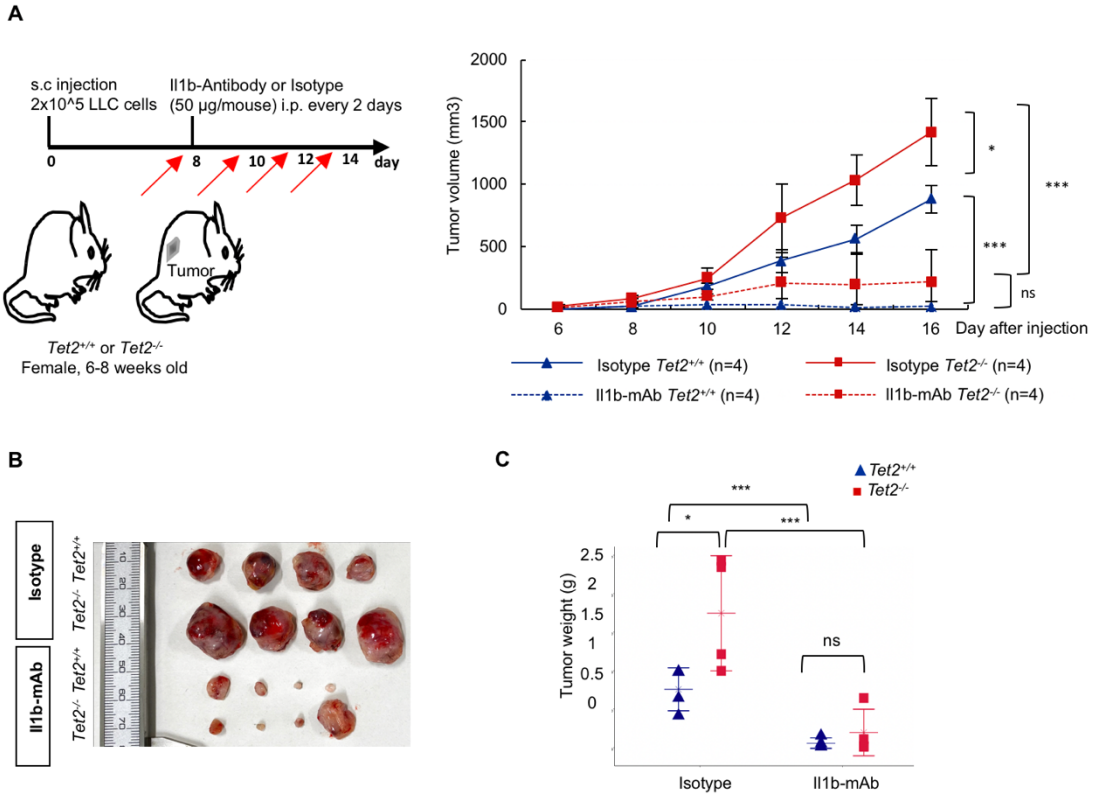

Figure 16. Administration of anti-Il1b antibody.

(A) Schematic showing time-line of injection of anti-Il1b antibody or isotype control into *Tet2*$^{-/-}$ or *Tet2*$^{+/+}$ mice harboring LLC cell tumors (left). Red arrows indicate the timing when we inject either anti-Il1b antibody or isotype. Tumor volume was measured by digital calipers and calculated as length x width x width x 0.52 after subcutaneous LLC cell injection into flanks of indicated mice after treatment with either anti-Il1b antibody or its isotype control (right). Mean ± s.d. is shown. Each group, n = 4. (B, C) Macroscopic analysis (B) and tumor weight (C) of groups shown in (A) at day 16.

I then evaluated S100a8 and S100a9 protein levels in plasma of tumor-bearing *Tet2*$^{-/-}$ and *Tet2*$^{+/+}$ mice with anti-Il1b antibody or isotype treatment (Fig. 17). S100a8 and

S100a9 protein levels were significantly higher in tumor-bearing *Tet2*$^{-/-}$ than in *Tet2*$^{+/+}$ mice ($p < 0.05$) as were found in Fig. 4B. Notably, both protein levels were significantly lower in anti-Il1b-treated group comparing to isotype-treated group in *Tet2*$^{-/-}$ mice (Fig. 17). Consequently, after the anti-Il1b antibody treatment, both protein levels were comparable between these genotypes (Fig. 17).

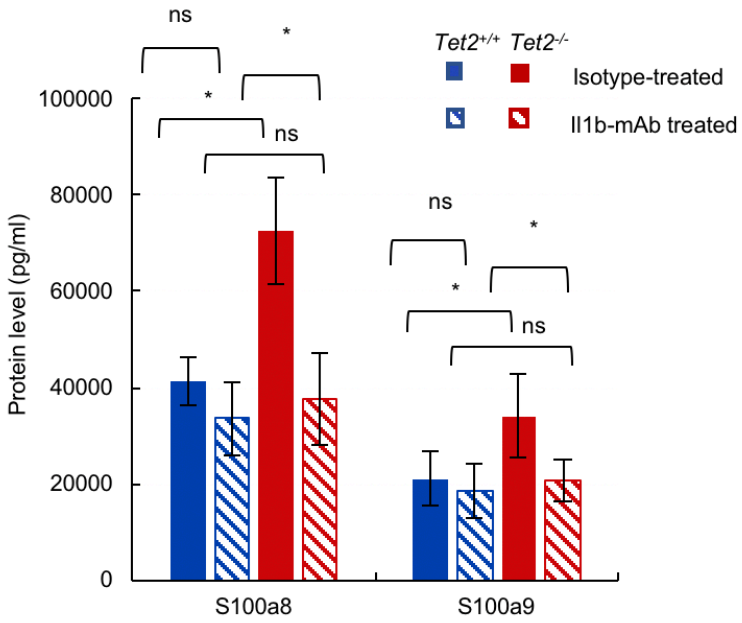

Figure 17. Administration of anti-Il1b antibody.

S100a8/S100a9 protein levels in plasma of either anti-Il1b antibody or its isotype control mice, based on ELISA. Each group, n=3. For all panels, *$p < 0.05$; **$p < 0.01$; ***$p < 0.005$; ns, not significant.

These data indicate that Il1b functions as an upstream signaling of S100a8/S100a9 in *Tet2*-deficent immune cells, and further the blockade of Il1b-S100a8/s100a9 signaling

effectively inhibits the growth of tumors generated in mice with *Tet2*-deficient immune cells.

4.7 Multiple Vegfa-related pathways are enriched in LLC cells sorted from tumors in *Tet2*$^{-/-}$ as compared to *Tet2*$^{+/+}$ mice

I next asked how S100a8/S100a9-Emmprin signaling might impact LLC tumors in *Tet2*$^{-/-}$ mice. Interestingly, growth of LLC cells *in vitro* was unchanged by S100a8/S100a9 treatment (Fig. 18A), suggesting that S100a9/S100a9 does not directly regulate LLC tumor growth. Thus to understand how S100a8/S100a9-Emmprin signaling initiated by *Tet2*-deficient immune cells might stimulate LLC growth in vivo, I performed WTA for LLC cells purified from tumors in *Tet2*$^{-/-}$ and *Tet2*$^{+/+}$ mice. PCA and unsupervised clustering heatmap analysis revealed a distinct gene expression pattern in LLC cells purified from *Tet2*$^{-/-}$ compared to *Tet2*$^{+/+}$ tumors (Figs. 18B, C). When I analyzed DEGs between *Tet2*-deficient and WT groups (FDR $p < 0.05$) (Figs. 18D, E), 318 genes were significantly upregulated and 192 downregulated in LLC cells purified from *Tet2*$^{-/-}$ tumors (Fig. 18F). Analysis of genes highly expressed in LLC cells purified *Tet2*$^{-/-}$ tumors revealed 77 genes showing at least a 2-fold change and 32 showing at least a 3-fold change (Fig. 18F). Notably, expression of *Vegfa*, which encodes a factor that stimulates angiogenesis, was highly upregulated in LLC cells from *Tet2*$^{-/-}$ tumors (Figs. 18D, E).

Consistent with flow cytometric analysis shown in Fig. 14B, *Emmprin* mRNA expression was higher in LLC cells in *Tet2*$^{-/-}$ compared to *Tet2*$^{+/+}$ tumors (FDR p < 0.005), while *Tlr4* and *Ager* mRNA expression were lower overall and comparable between genotypes (Fig. 18G).

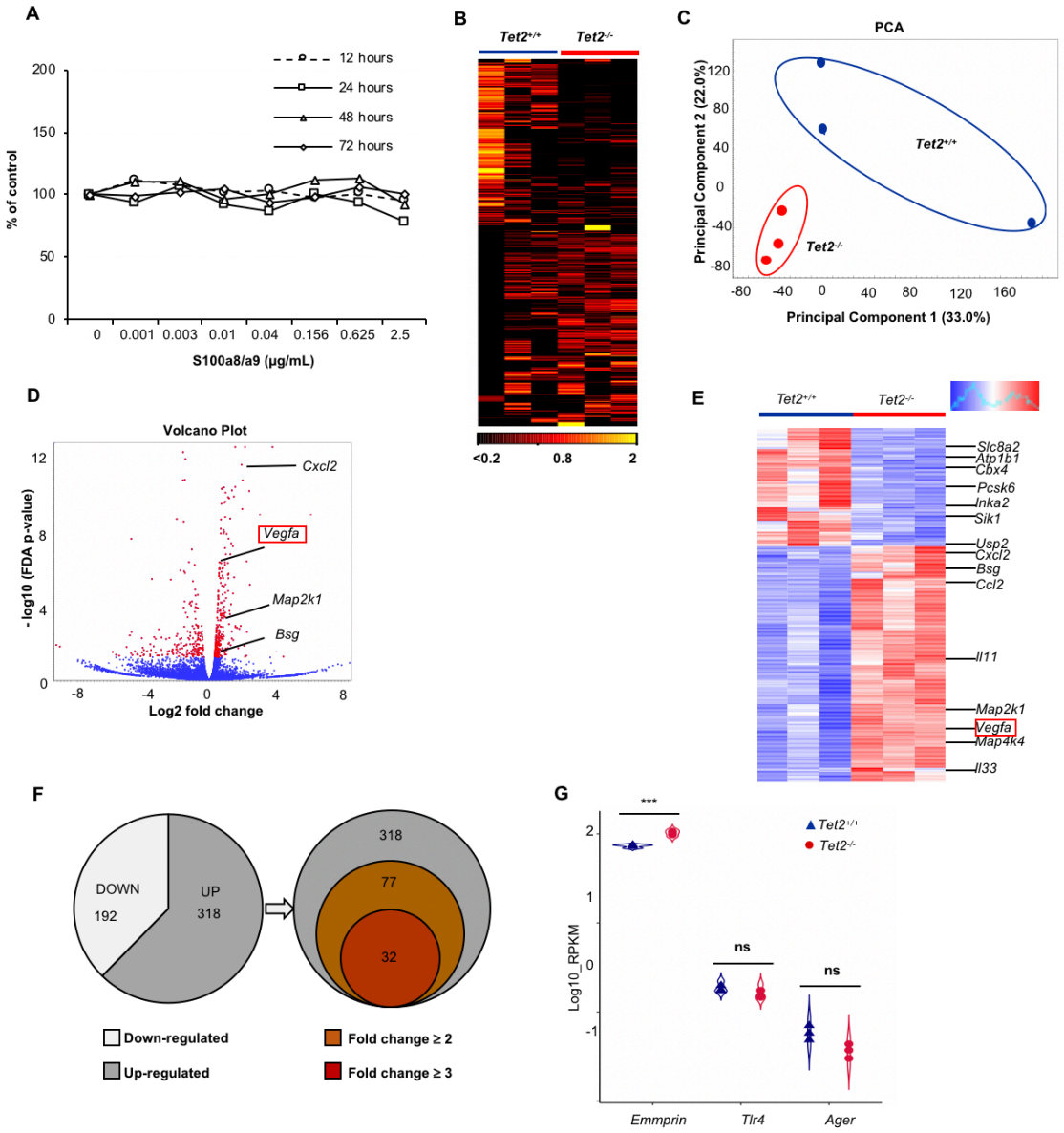

Figure 18. S100a8/a9 stimulations in LLC and WTA data of LLC cells.

(A) Growth of LLC cells treated in vitro with S100a8/a9 proteins at 12, 24, 48, or 72 hours. (B) Heatmap of unsupervised clustering of genes differentially expressed in LLC cells sorted from tumors in *Tet2*$^{-/-}$ mice versus those from tumors in *Tet2*$^{+/+}$ mice. (C) A PCA plot for WTA of LLC cells sorted from tumors in *Tet2*$^{-/-}$ (n=3) and *Tet2*$^{+/+}$ (n=3) mice. X- and Y- axes show respective percentages of variation of each principal component. (D) Volcano plot showing DEGs in LLC cells from tumors in *Tet2*$^{-/-}$ relative to *Tet2*$^{+/+}$ mice. (E) Heatmap of supervised clustering of DEGs between LLC cells from tumors in *Tet2*$^{-/-}$ compared to *Tet2*$^{+/+}$ mice (FDR $p < 0.05$). Colors from blue to red indicate differing gene expression from low to high. (F) Pie graph showing the proportion of up- (grey) or down- (white) genes with a FDR $p < 0.05$ in LLC cells from tumors in *Tet2*$^{-/-}$ relative to *Tet2*$^{+/+}$ mice (left). Venn diagram shows the number of upregulated genes only and indicated fold-changes (right). (G) Expression of *Bsg, Tlr4* and *Ager* from WTA of tumor-derived LLC cells.

Metascape analysis for genes highly expressed in LLC cells purified in *Tet2*$^{-/-}$ tumors indicated enrichment pathways related to blood vessel development, regulation of angiogenesis, regulation of the MAPK cascade and regulation of ERK1 and ERK2 signaling (Fig. 19 and Table 5).

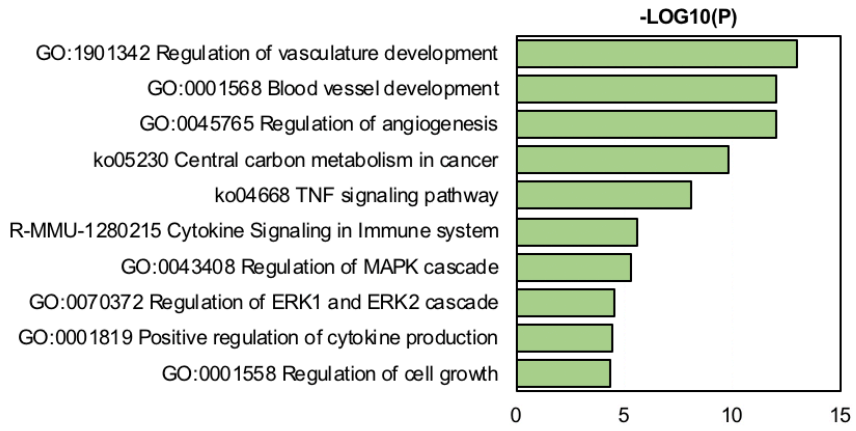

Figure 19. WTA data of LLC cells.

Metascape analysis of top 10 enrichment pathways based on genes upregulated in the *Tet2*$^{-/-}$ relative to *Tet2*$^{+/+}$ groups. Cut-off, FDR $p < 0.05$.

Table 5. Top 10 significantly enriched pathways from GO and KEGG enrichment analysis of WTA data of LLC cells.

GO	Description	LogP	Enrichment	Z-score
GO:1901342	regulation of vasculature development	-13	5.4	10
GO:0045765	regulation of angiogenesis	-12	5.6	10
GO:0001568	blood vessel development	-12	3.7	9.1
ko05230	Central carbon metabolism in cancer	-9.8	12	11
ko04668	TNF signaling pathway	-8.1	8.1	9.1
R-MMU-1280215	Cytokine Signaling in Immune system	-5.6	2.9	5.7
GO:0043408	regulation of MAPK cascade	-5.3	2.6	5.3
GO:0070372	regulation of ERK1 and ERK2 cascade	-4.6	3.4	5.3
GO:0001819	positive regulation of cytokine production	-4.5	2.8	5
GO:0001558	regulation of cell growth	-4.4	2.9	4.9

I then performed GSEA of WTA data to define pathways enriched in LLC cells in *Tet2*$^{-/-}$ tumors (Figs. 20A, B). Curated gene sets (C2) in the Molecular Signature Database (MSigDB) indicated significant enrichment of multiple pathways related to angiogenesis/Vegfa and ERK-MAP kinases in LLC cells purified from tumors in *Tet2*$^{-/-}$ mice (Figs. 20A, B).

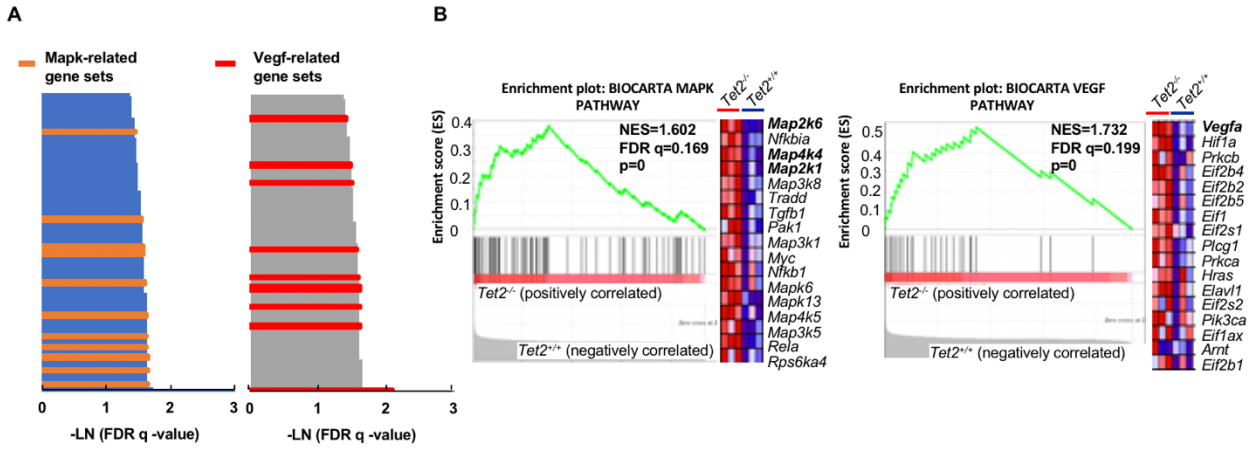

Figure 20. Multiple *Vegfa*-related pathways are enriched in LLC cells.

(A) Gene sets enriched in LLC cells from *Tet2*$^{-/-}$ relative to *Tet2*$^{+/+}$ mice. Orange bars, MAPK-related gene sets (left). Red bars, VEGF-related gene sets (right). Cut off, FDR q < 0.25; nominal p < 0.05. (B) Enrichment plots and heatmaps based on GSEA of BIOCATA MAPK (left) and BIOCARTA VEGF (right) pathways. Representative data from LLC cells was sorted from *Tet2*$^{+/+}$ (n=3) and *Tet2*$^{-/-}$ (n=3) mice.

4.8 Vegfa is a candidate effector of S100a8/S100a9 secreted from GMD

Based on the above findings, I hypothesized that S100a8/S100a9 stimulation might promote Vegfa expression by LLC cells. To assess this possibility, I treated LLC cells

grown *in vitro* with S100a8/S100a9 and measured both Vegfa mRNA and protein levels (Fig. 21A). S100a8/S100a9 treatment upregulated *Vegfa* mRNA expression in LLC cells relative to controls (Fig. 21B). I also observed high levels of Vegfa protein in supernatants of S100a8/S100a9-treated LLC cells relative to controls (Fig. 21C).

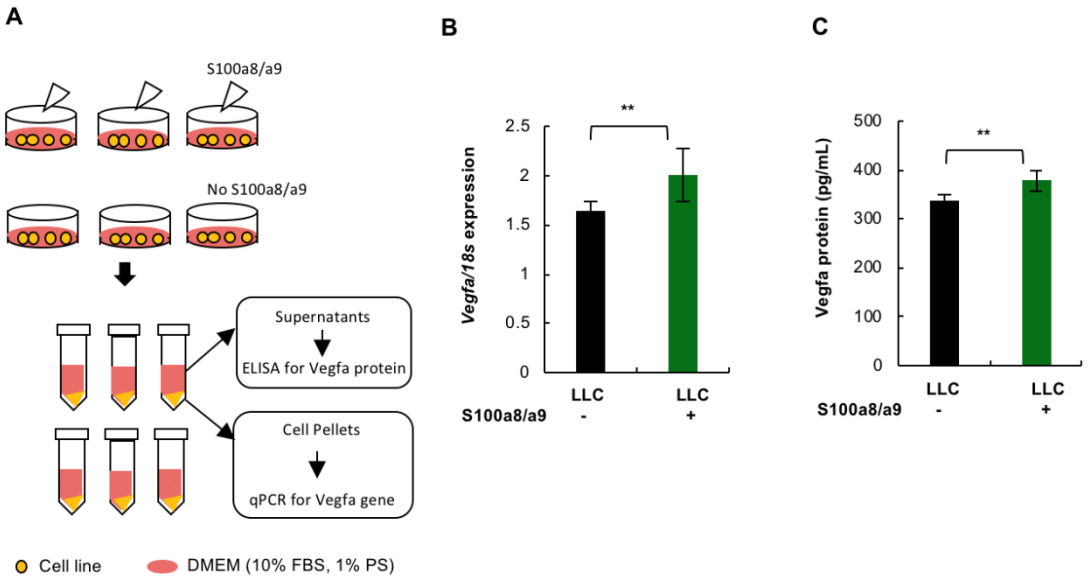

Figure 21. Vegfa protein secretions are stimulated by S100a/S100a9 in both mouse and human lung cancer cells.

(A) Experimental schema showing strategy to measure Vegfa protein and *Vegfa* gene in supernatants and cell pellets of LLC cells treated with S100a8/a9 proteins, respectively. (B) *Vegfa* expression normalized to *Rn18s* in LLC cells stimulated in vitro with S100a8/a9 proteins. For replicates of each group, n = 4. (C) Vegfa protein levels in supernatants of cells described in (E), as detected by ELISA. For replicates of each group, n = 4.

I then established co-cultures of LLCs plus either *Tet2*-deficient or WT GMD sorted from tumors and assessed Vegfa protein levels in supernatants from co-cultures as compared to LLCs cultured alone (Fig. 22A). Vegfa concentrations were significantly higher in supernatants from LLCs co-cultured with GMD regardless of their genotype (Fig. 22B). Furthermore, *Tet2*-deficient GMD had higher ability than WT GMD to stimulate Vegfa expression form LLC cells ($p < 0.05$) (Fig. 22B). Moreover, treatment of co-cultures with anti-Emmprin antibody decreased Vegfa protein levels in supernatants from both LLC/*Tet2*-deficient GMD and LLC/WT GMD sorted from tumors (Fig. 22C). These data suggest that Vegfa could be an effector of S100a8/S100a9 in this system.

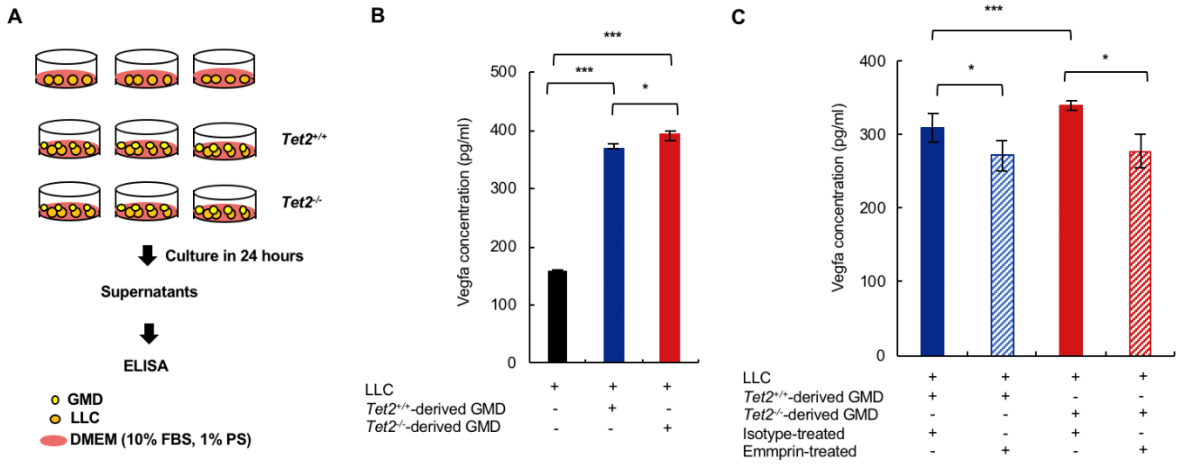

Figure 22. Co-culture and in vivo analysis of S100a8/S100a9-expressing myeloid cells effects on Vegfa expression.

(A) Experimental schema showing co-culture of LLC cells with GMD sorted from tumors. (B) Vegfa concentrations as detected by ELISA in supernatants (replicates, n=3) 24 hours after initiation of co-culture of LLC with *Tet2*-deficient or WT GMD. For all panels, *p < 0.05; **p < 0.01; ***p < 0.005; ns, not significant. (C) Anti-Emmprin or isotype control treatment of co-cultures described above followed by ELISA analysis of Vegfa protein in supernatants (replicates, n=3). For all panels, *p < 0.05; **p < 0.01; ***p < 0.005; ns, not significant.

Next, I examined S100A8/S100A9 expression in 43 human lung cancer lines using microarray data. Although a few cell lines harboring EGFR mutations (HCC827 and H1650) or ALK translocations (H2228) showed high S100A8/S100A9 mRNA expression levels, most expressed low levels of both S100A8 and S100A9 (Fig. 23A). I next treated the human lung cancer lines A549 and LC-Ad-1 with S100A8/S100A9 *in vitro* and assessed VEGFA protein levels in supernatants. Those levels significantly increased in both lines following S100A8/S100A9 treatment ($p < 0.05$) (Fig. 23B), supporting the idea that S100A8/S100A9 may upregulate VEGFA secretion by human lung cancer cells rather than only in mouse lung cancer cells represented by LLC.

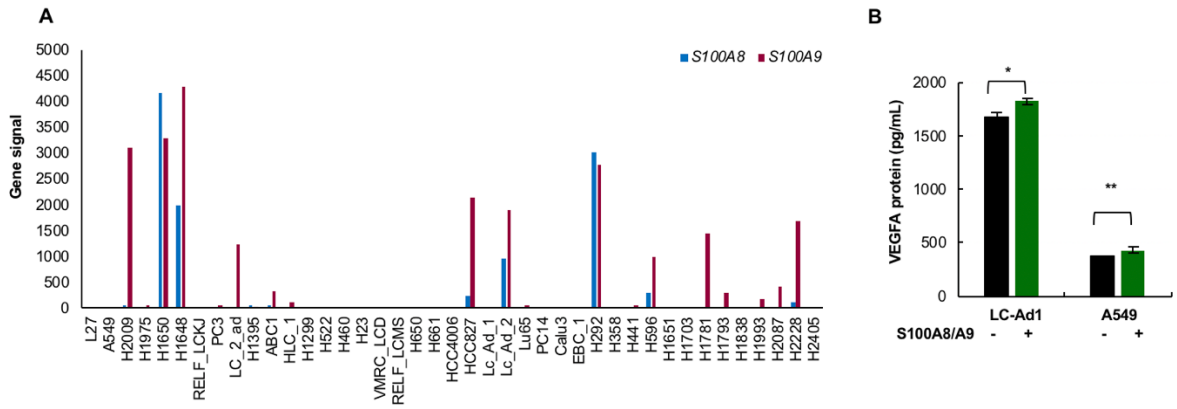

Figure 23. Microarray data of human lung cancer lines and S100A8/A9 stimulation.

(A) The signal of *S100A8* and *S100A9* from microarray data of 41 human cell lines. (B) VEGFA protein levels in supernatants of LC-Ad-1 or A549 cells treated in vitro with S100A8/A9 proteins, as detected by ELISA. For replicates of each group, n = 4.

4.9 LLC tumors in *Tet2*$^{-/-}$ mice exhibit enhanced vascularization relative to *Tet2*$^{+/+}$ tumors

Given that Vegfa promotes angiogenesis, I undertook histological and immunohistochemical comparison of vascular structures in LLC tumors in *Tet2*$^{-/-}$ mice with those in *Tet2*$^{+/+}$ mice. Based on HE staining, the area occupied by blood vessels in *Tet2*$^{-/-}$ tumors increased at 3-fold compared to that seen in *Tet2*$^{+/+}$ tumors ($p < 0.005$) (Figs. 24A, B). Accordingly, the area stained by an anti-CD31 antibody in tumor sections increased 3-fold in tumors from *Tet2*$^{-/-}$ as compared to *Tet2*$^{+/+}$ mice ($p < 0.05$) (Figs. 24C, D).

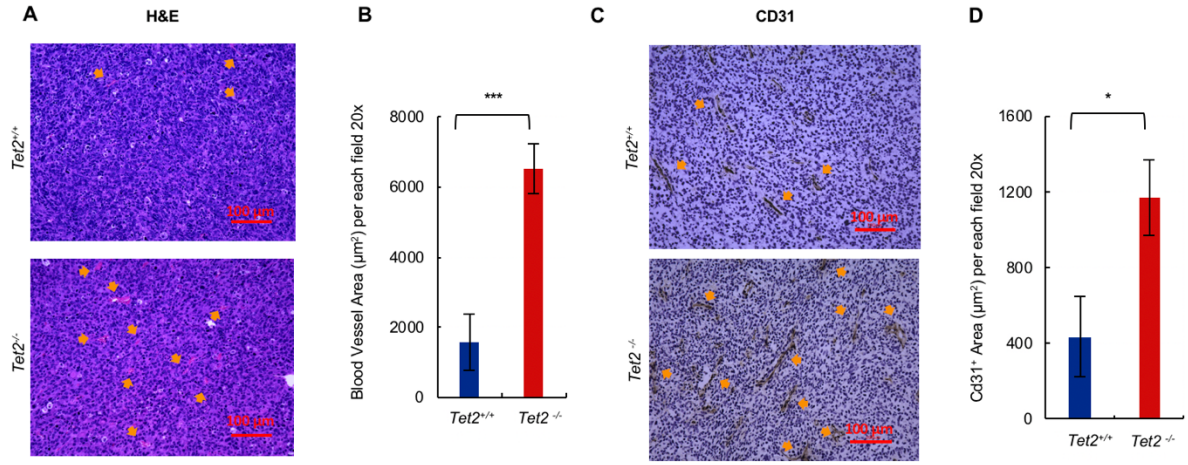

Figure 24. Vascular structure analysis.

(A) Hematoxylin-Eosin (HE) staining of tumor sections from *Tet2*$^{-/-}$ and *Tet*$^{+/+}$ mice (n = 3, each group). Orange arrows, blood vessels. Scale bars, 100 μm. (B) Blood vessel area per each field at 20x magnification (15 random fields of view per sample) in tumor sections from *Tet2*$^{-/-}$ (n=3) and *Tet2*$^{+/+}$ (n=3) mice. (C) Immunohistochemical staining of tumor sections from *Tet2*$^{-/-}$ (n=3) and *Tet2*$^{+/+}$ (n=3) mice with anti-Cd31 antibody. Orange arrows indicate Cd31^{+} area. (D) Cd31^{+} area per each field at 20x magnification (5 random fields of view per sample) in tumor sections from *Tet2*$^{-/-}$ (n=3) and *Tet2*$^{+/+}$ (n=3) mice.

4.10 Immunostaining of tumor tissues shows high S100a8/S100a9 expression in GMD from *Tet2*$^{-/-}$ mice

To compare localization of S100a8/S100a9 protein with GMD markers in tumors, I stained tumor sections from *Tet2*$^{-/-}$ and *Tet2*$^{+/+}$ mice with an antibody to Ly6g (a GMD marker) plus either anti-S100a8 or S100a9 antibodies. I observed an increase in large foci

(>1000 px^2) consisting of Ly6g-positive cells in tumor sections from *Tet2*$^{-/-}$ relative to *Tet2*$^{+/+}$ mice (Figs. 25A, B, D), and cells were also positive for S100a8 and S100a9 (Figs. 25A, B, E). Vegfa expression also increased in tumor sections in *Tet2*$^{-/-}$ compared to *Tet2*$^{+/+}$ mice (Figs. 25C, E). Vegfa-highly positive LLC cells exist surrounding Ly6g^{+} GMD large foci in tumor sections in *Tet2*$^{-/-}$ mice (Fig. 25C).

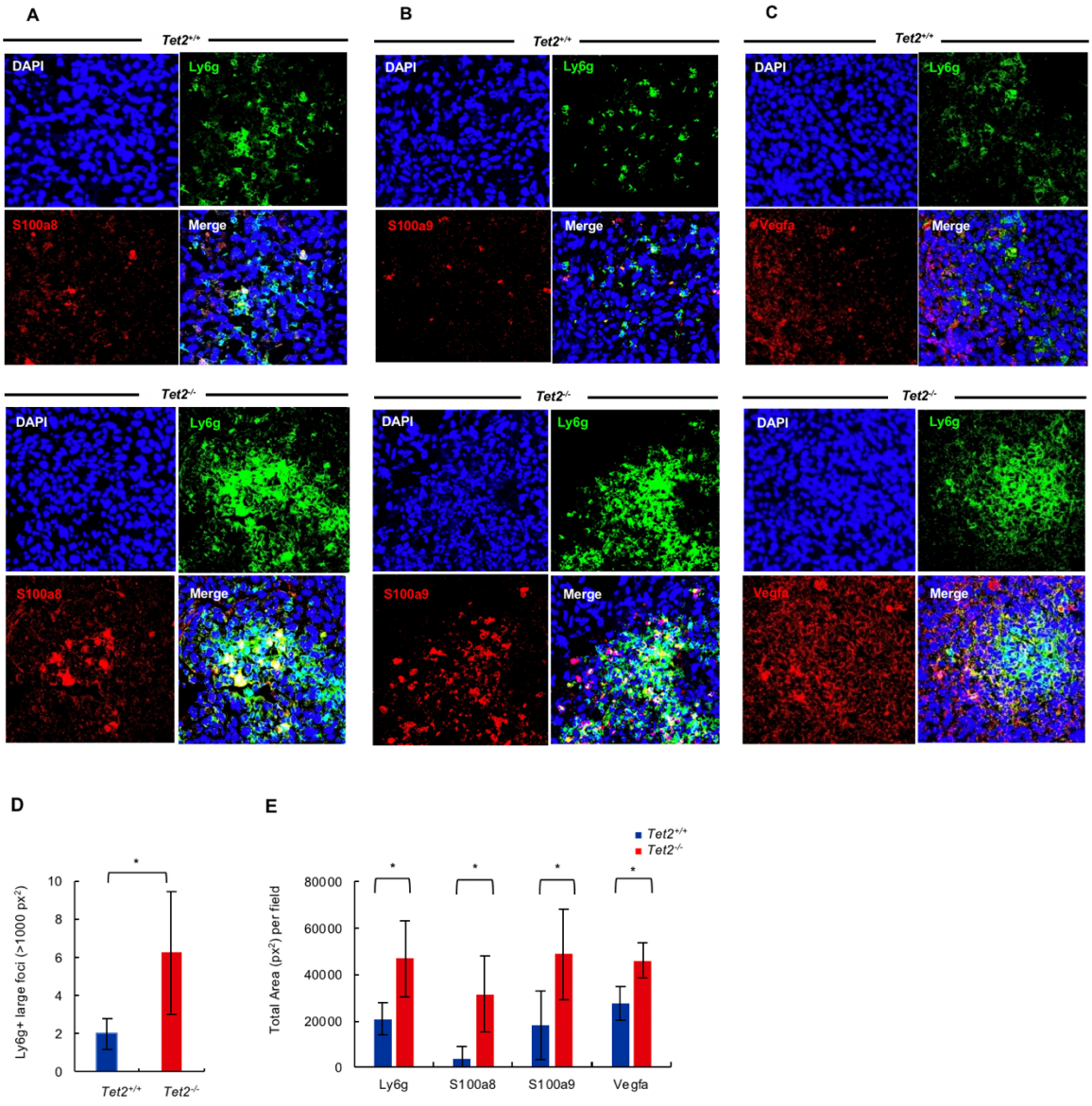

Figure 25. Immunofluorescent analysis of tumor sections.

(A) Tumor sections were stained for Ly6g plus S100a8. (B) Tumor sections were stained for Ly6g plus S100a9. (C) Tumor sections were stained for Ly6g plus Vegfa. DAPI served as a nuclear stain. Shown is representative data from tumor sections: *Tet2*$^{+/+}$, n=4; *Tet2*$^{-/-}$, n = 4. (D) The number of Ly6g^{+} foci, whose area are larger than 1000 px^2 per each field at 20x magnification in tumor sections from *Tet2*$^{-/-}$ (n=4) and *Tet2*$^{+/+}$ (n=4) mice. (E) Positive area (px^2) of Ly6g, S100a8, S100a9 and Vegfa per field at 20x magnification in tumor sections from *Tet2*$^{-/-}$ (n=4) and *Tet2*$^{+/+}$ (n=4) mice.

Then, I compared vascular structures in LLC tumors in *Tet2*$^{-/-}$ mice with those in *Tet2*$^{+/+}$ mice treated with anti-Emmprin antibody or isotype control. Based on HE staining, the area occupied by blood vessels in *Tet2*$^{-/-}$ tumors with anti-Emmprin group decreased at 2-fold compared to that seen in isotype group ($p < 0.05$). In *Tet2*$^{+/+}$ tumors, however, there was not significant difference between anti-Emmprin and isotype group, although the blood vessel area tended to be smaller in anti-Emmprin group than that in isotype group (Fig. 26).

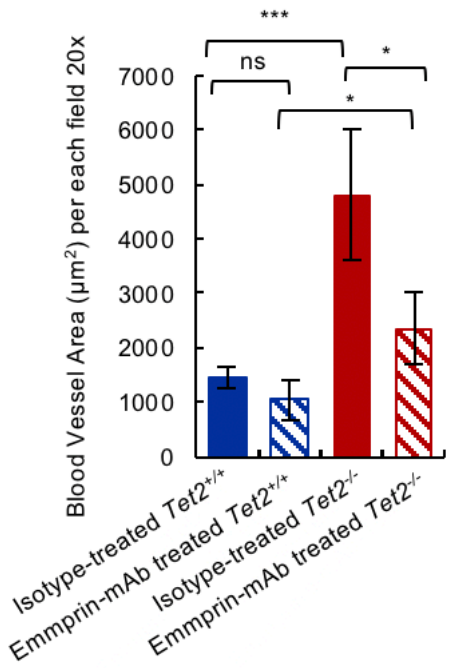

Figure 26. Vascular structure analysis.

Blood vessel area per each field at 20x magnification (5 random fields of view per sample) in tumor sections from *Tet2*$^{-/-}$ and *Tet2*$^{+/+}$ mice treated with either anti-Emmprin antibody or isotype control. Isotype-treated *Tet2*$^{+/+}$ (n=3), Isotype-treated *Tet2*$^{-/-}$ (n=5), Emmprin-mAb treated *Tet2*$^{+/+}$ (n=3) and Emmprin-mAb treated *Tet2*$^{-/-}$ (n=3).

These data suggest overall that *Tet2*-deficient GMD cells expressing S100a8 and S100a9 infiltrate tumors and may stimulate Vegfa production by LLC cells via its Emmprin receptor, enhancing tumor vascularization. Moreover, the blockade of S100a8/s100a9-Emmprin signaling effectively inhibits angiogenesis in tumors generated in immune cells with *Tet2* deletion.

4.11 Prognostic impact for human lung cancer patients

Using the Gene Expression Profiling Interactive Analysis (GEPIA) database, I then investigated the relationship between the genes encoding these mediators and their receptors and the prognosis of lung cancer patients: both adenocarcinoma and squamous cell carcinoma. In lung adenocarcinoma, patients showing high expression of *S100A8*, *S100A9*, *EMMPRIN*, or *VEGFA* showed a poor overall survival and disease-free survival, respectively (Fig. 27A). On the other hand, none of these factors served a predictive function in squamous cell lung cancer (Fig. 27B).

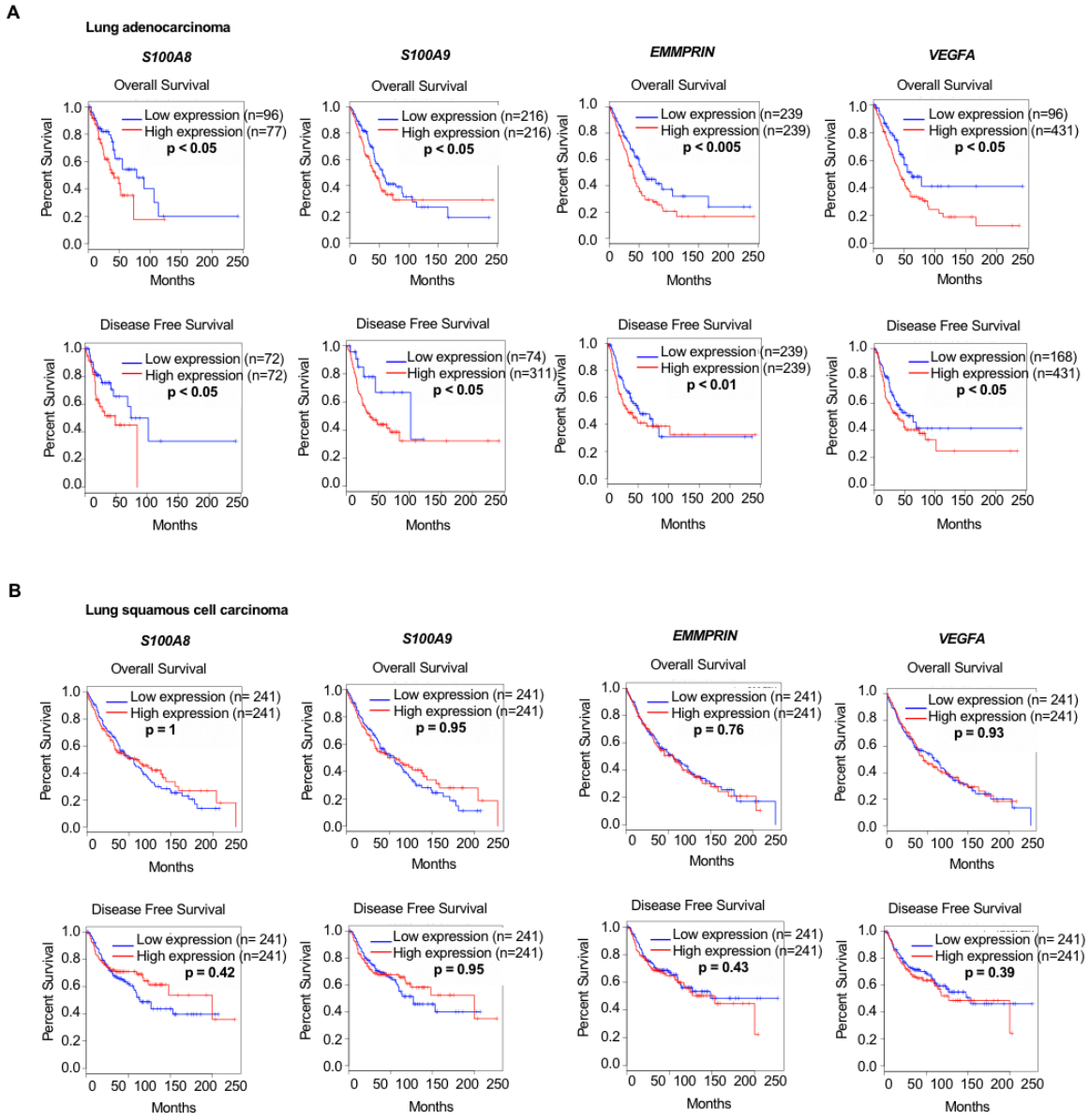

Figure 27. The clinical impact of *S100A8, S100A9, EMMPRIN*, or *VEGFA* expressions in lung cancer patients.

(A) Overall survival (OS) and disease-free survival (DFS) of patients with lung adenocarcinoma whose tumors show indicated *S100A8, S100A9, EMMPRIN,* or *VEGFA* expression. A log-rank test was applied

for statistical analysis. (B) OS and DFS comparable to that described in (A) but performed with patients with lung squamous cell carcinoma. A log-rank test was applied for statistical analysis.

5. DISCUSSION

Here, I present evidence that signaling through the S100a8/S100a9-Emmprin-Vegfa axis is essential for progression of a lung cancer model established in a microenvironment of *Tet2*-deficient immune cells. Specifically, I propose that S100a8/S100a9 secreted from *Tet2*-deficient GMD stimulates the Emmprin receptor expressed on lung cancer cells, which then secrete Vegfa, further promoting tumor angiogenesis. Notably, pathway analysis indicates that Il1b signaling serves as an upstream regulator of S100a8/S100a9 in *Tet2*-deficent GMD.

TET2 encodes a dioxygenase catalyzing 5-methylcytosine (5mC) into 5-hydroxymethylcytosine (5hmC), and then to 5-formylcytosine (5fC) and 5-carboxylcytosine (5caC). TET2 protein plays roles in a variety of epigenetic regulations, such as DNA demethylation process.[10, 12, 20] *Tet2* deficiency has been reported to result in loss of hypermethylation, leading to global change in gene expressions. It remains to be elucidated if upregulation of mediators in *Tet2*–deficient immune cells in our studies is the direct effect of dynamic change in DNA modification status.

Loss of function *TET2* mutations are found in a wide variety of blood cancers in addition to clonal hematopoiesis.[12] *TET2* mutations may modify microenvironment through alternating related immune cells and promoting the increase of proinflammatory

gene expression such as *IL1B*, *TNF* and *IL6*, then, progress MDS and AML.[2, 3, 21] Deletion of *Tet2* in the blood system resulting in myeloid cancer development after long latencies in mice, confirming its role as a tumor suppressor.[8, 12] In solid cancers, it is still controversial about downstream mechanisms of loss of function *TET2* in solid cancers although *TET2* mutations were found frequently in many tumor types.[2, 7] Recently, the analyses of melanoma[10] and liver cancer[11] models indicated that *Tet2*-deficient MDSCs modulate cancer progression by altering T cell-mediated immunity, although they played opposite roles in T-cell recruitment in each model. Intriguingly, my findings in a lung cancer model strongly suggest that *Tet2*-deficient myeloid cells, specially GMD alter activity of a vascular niche for tumor cells rather than directly altering T-cell mediated immunity. Overall, these data suggest that the effects of *TET2*-mutated clonal hematopoiesis in development of solid tumors is context-dependent.

Among of a variety of markers encoding secreted proteins determined from transcriptome analysis of immune cells, *S100a8/S100a9* exhibits the predominant expression in *Tet2*-deficent GMD. In many previous studies, it was shown that S100a8 and S100a9, both S100 family proteins, are primarily secreted by myeloid lineage cells and biochemically form a heterodimer [17, 18, 22]. S100A8/S100A9 proteins reportedly modulates secretion of various proinflammation cytokines such as IL-8, IL-6, and IL-1β

or functions as a transcriptional coactivator in the nucleus in vito[18, 23, 24]. Currently, the high levels of S100a8/S100a9 were found some non-cancer diseases such as cardiovascular or kidney renal injury which exist of CH mutations were suggested leading to severe condition of disease.[25, 26] Especially, *Tet2* deficiency exacerbates renal ischemia-reperfusion injury in murine kidney with higher expression levels of *S100a8/S100a9* in comparison with WT group.[25] In solid cancers, oncogenic functions of S100A8/S100A9 were reported via evaluation of their activities to ability of invasion, migration and proliferation in various cancer cell lines, including breast, lung, gastric, and colon cancers[17, 24, 27, 28, 29]. In my lung cancer model, the data showed that not only *S100a8/S100a9* overexpressed in *Tet2*-deficient GMD cells, but also S100a8/S100a9 proteins elevated in plasmas of *Tet2*-deficient mice in comparison with WT mice. These data strongly indicated that S100a8/S100a9 might play essential mediators to support for tumor progression in appearance of *Tet2* deficiency.

When GMD activates as a niche function to tumor cells, a receptor is needed for signaling via mediators. Multiple S100a8/S100a9 receptors, including Emmprin, TLR4 and RAGE, have been identified and their differential activity may underlie the diverse roles played by S100a8/S100a9 in cancer progression, such as proliferation, metastasis, and angiogenesis [17, 18, 29]. In my model, Emmprin, rather than other well-known receptors

such as Tlr4 or Ager on lung cancer cells, highly expressed on LLC cells, might function as an S100a8/S100a9 receptor and could serve as a therapeutic target. Treatment with an anti-Emmprin antibody reducing tumors from Tet2-deficient mice demonstrated the key role of Emmprin in S100a8/S100a9 signaling to cancer cells and provided an effective blockade targeting to Emmprin receptor.

Emmprin is a cell-surface glycoprotein of the immunoglobulin superfamily [30], and its effectors are known to be matrix metalloproteinases (MMPs) [31] and VEGF [32], which, respectively, promote tumor invasion and angiogenesis. In my model, Vegfa rather than MMPs, mediates Emmprin signaling based on my observation that MMP expression levels in LLC cells were unchanged following *Tet2* deletion in immune cells (Table 6). The further gene ontology analysis found multiple enriched pathways related to *Vegfa,* confirming a crucial role to enhance tumor growth. Moreover, consequence of Vegfa secretion in leading angiogenesis was uncovered with increasing blood vessels in *Tet2*-deficient tumors relative to those in WT. Correspondingly, in vitro experiments with GMD and LLC co-culture in the anti-Emmprin antibody exist contributed more evidences to consolidate S100a8/S100a9-Emmprin-Vegfa signaling from GMD to LLC in tumors of *Tet2*-deficient mice.

Table 6. WTA indicated gene expression of MMPs in LLC.

Gene name	WT78-LLC_R1 (paired) (GE) - RPKM	WT83-LLC_R1 (paired) (GE) - RPKM	WT82-LLC_R1 (paired) (GE) - RPKM	KO79-LLC_R1 (paired) (GE) - RPKM	KO84-LLC_R1 (paired) (GE) - RPKM	KO81-LLC_R1 (paired) (GE) - RPKM
Mmp10	0	0.38141553	0.60154053	2.50124789	0.48660632	0.20807941
Mmp11	2.12912295	1.96690323	2.57126968	2.61113628	2.3356084	2.58605835
Mmp12	0.18677203	0.45622082	0.8489396	3.61938645	0.88802184	0.16670749
Mmp13	0.04767706	0.18428663	0.12492564	0.27497506	0.08089846	0.04468297
Mmp14	36.989615	32.2354347	31.5931334	44.3295353	32.1254212	36.9800087
Mmp15	0	0	0.01459845	0	0.00526391	0.00664557
Mmp16	0.08015144	0	0.00233785	0	0	0.00292667
Mmp17	0	0.0191762	0.00212234	0	0	0.00797065
Mmp19	6.12660585	3.94092793	3.61365111	4.61907934	5.64401149	5.45526013
Mmp1a	0	0.08112618	0.09090917	0.09441807	0.09348388	0.05058057
Mmp1b	0	0.16997866	0.08935928	0.25362607	0.08394471	0.11775371
Mmp2	12.9593779	13.0164556	14.9160004	23.6692744	14.1254292	14.0829473
Mmp20	0	0	0.00414653	0	0.00411168	0.01557272
Mmp21	0	0.02209357	0.0146713	0	0	0
Mmp23	0	0.14313057	0.1188079	0.06150697	0.06597328	0.22012306
Mmp24	0.01973073	0.15253078	0.27696091	0.14338296	0.160072	0.21001234
Mmp25	0	0.00774087	0.0102807	0.03880866	0.0101943	0.02895769
Mmp27	0	0	0.00616726	0	0	0
Mmp28	2.76898363	1.69681401	1.78767165	2.04883088	1.13521096	1.30432822
Mmp3	7.8073106	10.0630246	11.9609379	43.8229848	16.0365158	5.26275702
Mmp7	0	0	0	0.0137642	0	0
Mmp8	0.1051058	0	0	0	0	0
Mmp9	0.63158283	0.31736426	0.45594253	0.19670161	0.30944471	0.26382713

I further demonstrated that administration of an antibody against Il1b, a candidate upstream of S100a8/S100a9 in *Tet2*-deficient GMD by pathway analysis actually

antagonized lung cancer progression and decreased S100a8/S100a9 production. Notably, anti-IL1b antibody was shown to decrease incidence and mortality of lung cancer in patients with atherosclerotic disease in CANTOS trial[33], primarily examining the effect of anti-IL1b antibody for cardiovascular events for >10,000 patient [34]. Although clonal hematopoiesis was not examined in the CANTOS study, *TET2*-mutated clonal hematopoiesis has been shown to play roles in atherosclerotic disease in both human [35] and mouse studies [36]. My data may provide the functional evidence of IL1b in lung cancer progression in patients accompanying *TET2*-mutated clonal hematopoiesis.

Last but not least, my findings showed the clinical impact that the highly expressions of *S100A8, S100A9, EMMRPIN* and *VEGFA* lead to poor survival prognosis in lung adenocarcinoma, but no significant prediction in squamous cell lung cancer using GEPIA database. This finding indicated that S100A8/S100A9-EMMPRIN-VEGFA signaling might be specific in lung adenocarcinoma, but not in squamous cell lung cancer. Overall, my finding supports more proofs to a prospective therapeutic via the signaling relating to these genes in patients with *TET2*-mutated clonal hematopoiesis, which clinical impact is still concerned.

There are still limitations in my study. First, I analyzed the role of *Tet2*-deficient immune cells in cancer progression but did not address their potential impact on

metastasis, or resistance to anti-cancer drugs or immune-checkpoint inhibitors. Second, using a cell line restricted reliability of my study, especially demonstrating the consistence from mouse model to human clinical impact. Lastly, the roles of mutations in genes other than *TET2* in clonal hematopoiesis remain to be elucidated. Therefore, it is necessary to have further studies in patients with *TET2*-mutated clonal hematopoiesis to observe effective impact.

6. CONCLUSION

The study suggests a novel role of *TET2*-mutated clonal hematopoiesis in cancer progression. In mouse model, *Tet2*-deificient immune cells promote lung cancer progression through IL-1β-S100a8/S100a9-Emmprin-Vegfa axis and even provides a novel therapeutic target (Fig. 28).

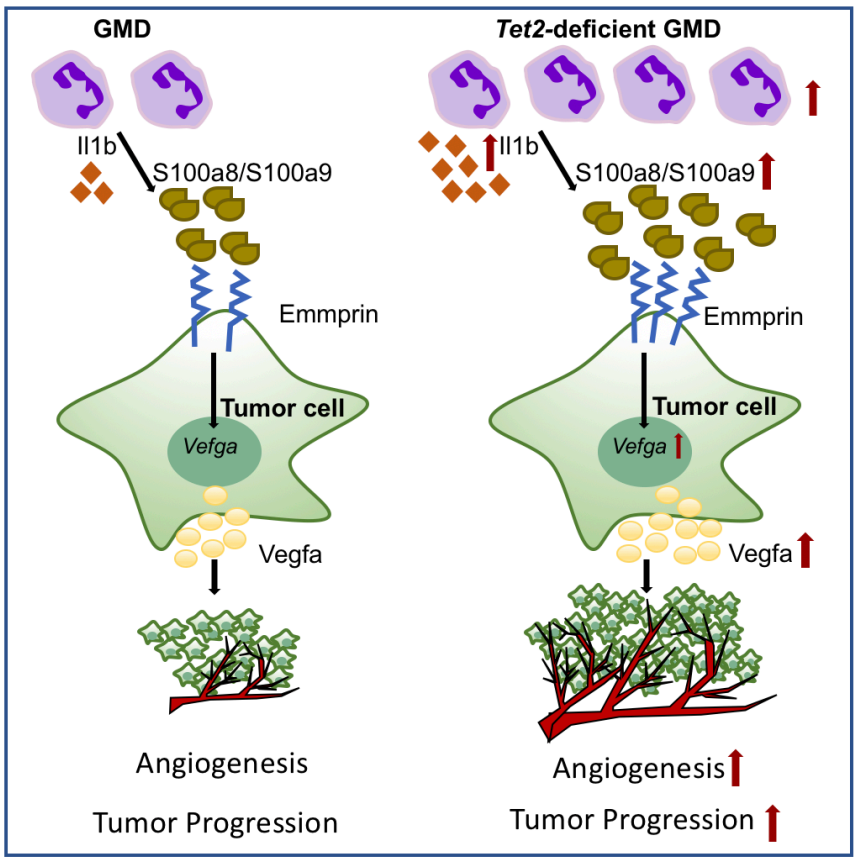

Figure 28. The scheme of a mechanism of *Tet2*-deficient immune cells derived from clonal hematopoiesis function as microenvironmental cells supporting lung cancer development.

Acknowledgment

Throughout over 4 years in Tsukuba for PhD program I received a great deal of support and assistance.

First of all, I would like to thank my supervisor, Professor Shigeru Chiba, taught me a huge of invaluable knowledge in science research, career orientation as well as helped me to overcome difficulties along my PhD life. I am really grateful about everything.

I would also like to thank my co-supervisor, Associate Professor Mamiko Sakata-Yanagimoto, directly formulated the research questions and methodology. Your insightful feedback sharpened my thinking and pushed my skills to a higher level. I am always grateful about your dedicated instruction bringing me up in science field and in normal life as well.

I would like to thank all senior doctors helped me deal with issues of the research project. Eventually, I had good enough data for a publication.

I would like to thank all patient support from Hematology Lab members. You are always willing to assist me doing the research project.

I want to show my deepest gratitude to my husband P.C.T, my little daughter P.Y.M, my mother N.T.Q, my mother in-law N.T.D.N as well as all my pretty sisters. You always stay beside me to make me happy and optimistic.

I would like to thank all my kind friends, Vietnamese, Japanese, Nepalese as well as others. I highly appreciate our friendship in support all life issues, not only living conditions but also metal support.

I would like to express my sincere gratitude to the Japanese Government for providing MEXT Scholarship to support finance to me to be able to finish PhD program.

University of Tsukuba, August 16th, 2021

Nguyen Thi Minh Yen

7. REFERENCES

1. Silver, A.J., Bick, A.G. & Savona, M.R. Germline risk of clonal haematopoiesis. *Nat Rev Genet* **22**, 603-617 (2021).

2. Jaiswal, S. *et al.* Age-Related Clonal Hematopoiesis Associated with Adverse Outcomes. *N Engl J Med* (2014).

3. Genovese, G. *et al.* Clonal hematopoiesis and blood-cancer risk inferred from blood DNA sequence. *N Engl J Med* **371**, 2477-2487 (2014).

4. Saiki, R. *et al.* Combined landscape of single-nucleotide variants and copy number alterations in clonal hematopoiesis. *Nat Med* **27**, 1239-1249 (2021).

5. Bejarano, L., Jordão, M.J.C. & Joyce, J.A. Therapeutic Targeting of the Tumor Microenvironment. *Cancer Discov* **11**, 933-959 (2021).

6. Gabrilovich, D.I. Myeloid-Derived Suppressor Cells. *Cancer Immunol Res* **5**, 3-8 (2017).

7. Coombs, C.C. *et al.* Therapy-Related Clonal Hematopoiesis in Patients with Non-hematologic Cancers Is Common and Associated with Adverse Clinical Outcomes. *Cell Stem Cell* **21**, 374-382.e374 (2017).

8. Park, S.J. & Bejar, R. Clonal hematopoiesis in cancer. *Exp Hematol* **83**, 105-112 (2020).

9. Nguyen, T.B. *et al.* Identification of cell-type-specific mutations in nodal T-cell lymphomas. *Blood Cancer J* **7**, e516 (2017).

10. Pan, W. *et al.* The DNA Methylcytosine Dioxygenase Tet2 Sustains Immunosuppressive Function of Tumor-Infiltrating Myeloid Cells to Promote Melanoma Progression. *Immunity* **47**, 284-297.e285 (2017).

11. Li, S. *et al.* TET2 promotes anti-tumor immunity by governing G-MDSCs and CD8. *EMBO Rep* **21**, e49425 (2020).

12. Jiang, S. Tet2 at the interface between cancer and immunity. *Commun Biol* **3**, 667 (2020).

13. Quivoron, C. *et al.* TET2 inactivation results in pleiotropic hematopoietic abnormalities in mouse and is a recurrent event during human lymphomagenesis. *Cancer Cell* **20**, 25-38 (2011).

14. Fuster, J.J. *et al.* TET2-Loss-of-Function-Driven Clonal Hematopoiesis Exacerbates Experimental Insulin Resistance in Aging and Obesity. *Cell Rep* **33**, 108326 (2020).

15. Kuhn, R., Schwenk, F., Aguet, M. & Rajewsky, K. Inducible gene targeting in mice. *Science* **269**, 1427-1429 (1995).

16. Butler, A., Hoffman, P., Smibert, P., Papalexi, E. & Satija, R. Integrating single-cell transcriptomic data across different conditions, technologies, and species. *Nat Biotechnol* **36**, 411-420 (2018).

17. Tomonobu, N., Kinoshita, R. & Sakaguchi, M. S100 Soil Sensor Receptors and Molecular Targeting Therapy Against Them in Cancer Metastasis. *Transl Oncol* **13**, 100753 (2020).

18. Pruenster, M., Vogl, T., Roth, J. & Sperandio, M. S100A8/A9: From basic science to clinical application. *Pharmacol Ther* **167**, 120-131 (2016).

19. Bullock, B.L. *et al.* Tumor-intrinsic response to IFNγ shapes the tumor microenvironment and anti-PD-1 response in NSCLC. *Life Sci Alliance* **2** (2019).

20. Chiba, S. & Sakata-Yanagimoto, M. Advances in understanding of angioimmunoblastic T-cell lymphoma. *Leukemia* **34**, 2592-2606 (2020).

21. Ferrone, C.K., Blydt-Hansen, M. & Rauh, M.J. Age-Associated. *Int J Mol Sci* **21** (2020).

22. Wang, S., Song, R., Wang, Z., Jing, Z. & Ma, J. S100A8/A9 in Inflammation. *Front Immunol* **9**, 1298 (2018).

23. Simard, J.C. *et al.* S100A8 and S100A9 induce cytokine expression and regulate the NLRP3 inflammasome via ROS-dependent activation of NF-κB(1.). *PLoS One* **8**, e72138 (2013).

24. Song, R. & Struhl, K. S100A8/S100A9 cytokine acts as a transcriptional coactivator during breast cellular transformation. *Sci Adv* **7** (2021).

25. Yan, H. *et al.* Ten-eleven translocation methyl-cytosine dioxygenase 2 deficiency exacerbates renal ischemia-reperfusion injury. *Clin Epigenetics* **12**, 98 (2020).

26. Pardali, E., Dimmeler, S., Zeiher, A.M. & Rieger, M.A. Clonal hematopoiesis, aging, and cardiovascular diseases. *Exp Hematol* **83**, 95-104 (2020).

27. Kwon, C.H., Moon, H.J., Park, H.J., Choi, J.H. & Park, D.Y. S100A8 and S100A9 promotes invasion and migration through p38 mitogen-activated protein kinase-dependent NF-κB activation in gastric cancer cells. *Mol Cells* **35**, 226-234 (2013).

28. Ichikawa, M., Williams, R., Wang, L., Vogl, T. & Srikrishna, G. S100A8/A9 activate key genes and pathways in colon tumor progression. *Mol Cancer Res* **9**, 133-148 (2011).

29. Bresnick, A.R., Weber, D.J. & Zimmer, D.B. S100 proteins in cancer. *Nat Rev Cancer* **15**, 96-109 (2015).

30. Hibino, T. *et al.* S100A9 is a novel ligand of EMMPRIN that promotes melanoma metastasis. *Cancer Res* **73**, 172-183 (2013).

31. Guo, H., Zucker, S., Gordon, M.K., Toole, B.P. & Biswas, C. Stimulation of matrix metalloproteinase production by recombinant extracellular matrix metalloproteinase inducer from transfected Chinese hamster ovary cells. *J Biol Chem* **272**, 24-27 (1997).

32. Tang, Y. *et al.* Extracellular matrix metalloproteinase inducer stimulates tumor angiogenesis by elevating vascular endothelial cell growth factor and matrix metalloproteinases. *Cancer Res* **65**, 3193-3199 (2005).

33. Ridker, P.M. *et al.* Effect of interleukin-1β inhibition with canakinumab on incident lung cancer in patients with atherosclerosis: exploratory results from a randomised, double-blind, placebo-controlled trial. *Lancet* **390**, 1833-1842 (2017).

34. Ridker, P.M. *et al.* Antiinflammatory Therapy with Canakinumab for Atherosclerotic Disease. *N Engl J Med* **377**, 1119-1131 (2017).

35. Jaiswal, S. *et al.* Clonal Hematopoiesis and Risk of Atherosclerotic Cardiovascular Disease. *N Engl J Med* **377**, 111-121 (2017).

36. Fuster, J.J. *et al.* Clonal hematopoiesis associated with TET2 deficiency accelerates atherosclerosis development in mice. *Science* **355**, 842-847 (2017).

SOURCE

Yen T.M. Nguyen, Manabu Fujisawa, Tran B. Nguyen, Yasuhito Suehara, Tatsuhiro Sakamoto, Ryota Matsuoka, Yoshiaki Abe, Kota Fukumoto, Keiichiro Hattori, Masayuki Noguchi, Daisuke Matsubara, Shigeru Chiba, and Mamiko Sakata-Yanagimoto. *Tet2*-deficency in immune cells exacerbates tumor progression by increasing angiogenesis in a lung cancer model. Cancer Science. Published online: Date.2021.10.17